Ontogeny of a subtidal point bar in the microtidal Venice Lagoon (Italy) revealed by three-dimensional architectural analyses

ELENA BELLIZIA* (iD), SANDRA DONNICI†, FANTINA MADRICARDO‡,
ALVISE FINOTELLO§, ANDREA D'ALPAOS* and MASSIMILIANO GHINASSI* (iD)
*Department of Geosciences, University of Padova, Via G. Gradenigo 6, Padova, IT-35131, Italy
(E-mail: elena.bellizia@phd.unipd.it)
†Institute of Geosciences and Earth Resources (IGG), National Research Council of Italy (CNR), Via G. Gradenigo 6, Padova, IT-35131, Italy
‡Institute of Marine Sciences (ISMAR), National Research Council of Italy (CNR), Tesa 104 – Arsenale, Castello 2737/F, Venezia, 30122, Italy
§Department of Environmental Sciences, Informatics, and Statistics, Ca' Foscari University of Venice, via Torino 155, Mestre, Venice, 30172, Italy

Associate Editor – Charlie Bristow

ABSTRACT

Sedimentological and architectural features of meandering subtidal channels are relatively unexplored, and their deposits are commonly investigated based on facies models set up for intertidal meandering channels. The Venice Lagoon (northern Adriatic Sea, Italy) is affected by a micro-tidal regime and hosts a dense network of active and buried tidal channels. It represents an excellent natural laboratory to improve the current knowledge on subtidal meander morphodynamics and related deposits. In this study, the integration of high-resolution geophysical images and core data allows reconstruction of the architectural three-dimensional model of a meandering subtidal palaeochannel, which is buried below a modern subtidal flat. The study palaeochannel was 35 m wide and 3 m deep, and formed three adjacent meander bends and related point bars. A detailed three-dimensional architectural reconstruction was carried out for deposits associated with one of these meander bends, that was crossed by a minor, low-sinuosity channel with two minor bank-attached bars. This reconstruction highlights that the study point bar has a horseshoe shape, which arose from the onset of bar accretion from an already-sinuous channel. Reconstructed growth stages of the studied bends show that point-bar accretion can follow different styles of planform transformation, also experiencing simultaneously landward (or seaward) deposition according to the dominant flow direction (i.e. local tidal asymmetry). The analyses show that planform transformations occurred in parallel with elevation changes of the related channel thalweg, which shaped pools with geometry varying with the radius of curvature of the bend. The present study highlights the relevance of high-resolution three-dimensional reconstructions to link palaeomorphodynamic processes with related sedimentary products.

Keywords Meander genesis, planform transformations, subtidal channel, tidal asymmetry, tidal point bars.

INTRODUCTION

The study of meandering-channel evolution and related deposits is a fascinating issue of clastic sedimentology, especially for modern and ancient fluvial systems (Visher, 1964; Allen, 1965; Bluck, 1971; Brice, 1974; Jackson, 1976b; Willis, 1989; Bridge, 1993; Nicoll & Hickin, 2010; Smith *et al.*, 2011; Ielpi & Ghinassi, 2014). Starting from an almost straight or slightly sinuous planform, channels increase their sinuosity by migrating laterally on the floodplain and evolve according to a wide spectrum of planform transformations (Leopold & Wolman, 1960; Daniel, 1971; Brice, 1974; Jackson, 1976b; Lewin, 1976; Nanson & Page, 1983; Ghinassi *et al.*, 2014, 2016; Durkin *et al.*, 2017). The evolution of fluvial meandering channels produces laterally-extensive point-bar bodies, which can become important hydrocarbon reservoirs (for example, the McMurray Formation, Hubbard *et al.*, 2011; Fustic *et al.*, 2012), or targets for carbon capture and storage (Issautier *et al.*, 2014; Gershenzon *et al.*, 2015), and host most of the surficial aquifers in modern coastal plains (Clement & Barrash, 2006; Fabbri & Ortombina, 2012).

Meandering channels also occur in subaqueous settings, both as well-known turbiditic channels (e.g. Posamentier, 2003; Kolla & Posamentier, 2007; Janocko *et al.*, 2013) and as less-documented subtidal channels (e.g. Flemming, 2012) in lagoons and estuaries. Most of the current knowledge on tidal meanders and related point bars has been developed for intertidal meanders, which have been commonly assumed to slowly migrate laterally (Gabet, 1998) and generate tabular point-bar bodies (Bridges & Leeder, 1976; Barwis, 1977). Distinctive sedimentary features of these bar deposits are classically considered to be (Allen, 1982): (i) a shell-rich channel lag; (ii) bedforms diagnostic of bidirectional flows; (iii) alternation between sandy and silty layers; and (iv) intense bioturbation. Recent studies provided new insights on the morphometry and sedimentology of intertidal meanders (Fagherazzi & Gabet, 2004; Pearson & Gingras, 2006; Choi, 2011; Hughes, 2012; Choi *et al.*, 2013; Choi & Jo, 2015; Brivio *et al.*, 2016; Ghinassi *et al.*, 2018b; Cosma *et al.*, 2019, 2021; Finotello *et al.*, 2019), revealing that: (i) intertidal-meander migration rates are comparable to those of their fluvial counterparts, once properly normalized by the channel width (Finotello *et al.*, 2018); (ii) geometry of intertidal point bars is the result of the interaction between channel-migration rate and aggradation rate of the surrounding marsh platform (Brivio *et al.*, 2016; Cosma *et al.*, 2019, 2021); (iii) morphometry of intertidal meanders can differ from that of their fluvial counterparts (Finotello *et al.*, 2019); and (iv) complex flow configurations, due to the occurrence of mutually evasive currents and recirculation zones, can prevent portions of bar deposits from experiencing bidirectional currents, thereby inhibiting the formation of bedforms retaining the signatures of bidirectional flows (Dalrymple & Choi, 2007; Li *et al.*, 2008; Choi *et al.*, 2013; Finotello *et al.*, 2020a).

Despite these recent new findings, several gaps still exist in the understanding of tidal meanders and the related point-bar deposits. One of these gaps is mostly due to the absence of scroll-bar patterns that typically characterize the present-day morphology of most tidal meanders worldwide. These patterns would allow for detailed reconstructions of meander planform evolution, in a fashion similar to fluvial meanders where well-developed scroll bars are widespread and clearly visible from aerial images (Brice, 1974; Nanson, 1980; Strick *et al.*, 2018). Indeed, correlations between planform evolution (i.e. scroll-bar pattern) and related point-bar geometries were carried out for fluvial meanders (Pranter *et al.*, 2007; Ghinassi *et al.*, 2013, 2014; Ielpi & Ghinassi, 2014; Ghinassi & Ielpi, 2015; Yan *et al.*, 2017, 2019; Willis & Sech, 2018a; Ghinassi *et al.*, 2019a; Parquer *et al.*, 2019) along with models concerning along-bend grain-size distribution (Purkait, 2002; Frings, 2008; Smith *et al.*, 2009, 2011; Bhattacharyya & Bhattacharya, 2015; Ghinassi & Ielpi, 2015; Clift *et al.*, 2019; Hagstrom *et al.*, 2019). Comparable insights are conversely missing for intertidal meanders, whose planform evolution has been inferred only for short time intervals (Choi *et al.*, 2013; Ghinassi *et al.*, 2018b) and for which the spatial distribution of sediment grain size was mainly investigated with vertical, rather than along-channel, trends (de Mowbray, 1983; Dalrymple *et al.*, 1990; Pearson & Gingras, 2006; Choi, 2011; Choi *et al.*, 2013; Choi & Jo, 2015).

Knowledge gaps are even more relevant for subtidal channels, which have been investigated by few studies (e.g. La Croix & Dashtgard, 2015; Ghinassi *et al.*, 2019b) despite their widespread presence in coastal environments [for example, the Geum River estuary (Korea) and Hammocks Beach State Park, North Carolina (USA)]. Subtidal meandering channels can be found in the most

seaward portion of tidal basins (Rieu *et al.*, 2005), where current velocities are higher because of the inlets, and they are permanently submerged. They usually develop on top of tidal flood deltas and their hydrodynamics is complex (Rieu *et al.*, 2005; Ghinassi *et al.*, 2019b) since the flow within the channels can be influenced by the currents flowing on the surrounding subtidal platforms and by the wind-induced wave winnowing (Carniello & Defina, 2012; Tommasini *et al.*, 2019). Subtidal meanders can migrate laterally accumulating point bars that thereby do not experience any subaerial exposure. Therefore, defining the internal architecture and the sediment distribution within subtidal point-bar deposits is a critical step to deepen current knowledge on the genesis and evolution of subtidal meanders.

The present study aims at improving current understanding on the morphodynamic evolution and internal architecture of subtidal point-bar deposits, focusing on a Holocene tidal meandering channel cutting through a subtidal mudflat of the northern Venice Lagoon (Adriatic Sea, Italy; Fig. 1). With its complex network of tidal channels developed in a microtidal regime, the Venice Lagoon represents a key site to study facies distribution and architectural features of a microtidal system, where effects of tidal currents are amplified by meteorological forcings. By integrating geophysical and sedimentological data with morphological characteristics of a previously-detected Holocene palaeochannel (Madricardo *et al.*, 2007), this work reconstructs the detailed 3D architectural model of a subtidal meander and investigates: (i) the onset of tidal meanders and following planform transformations; and (ii) the related changes in bend morphometry and channel bathymetry.
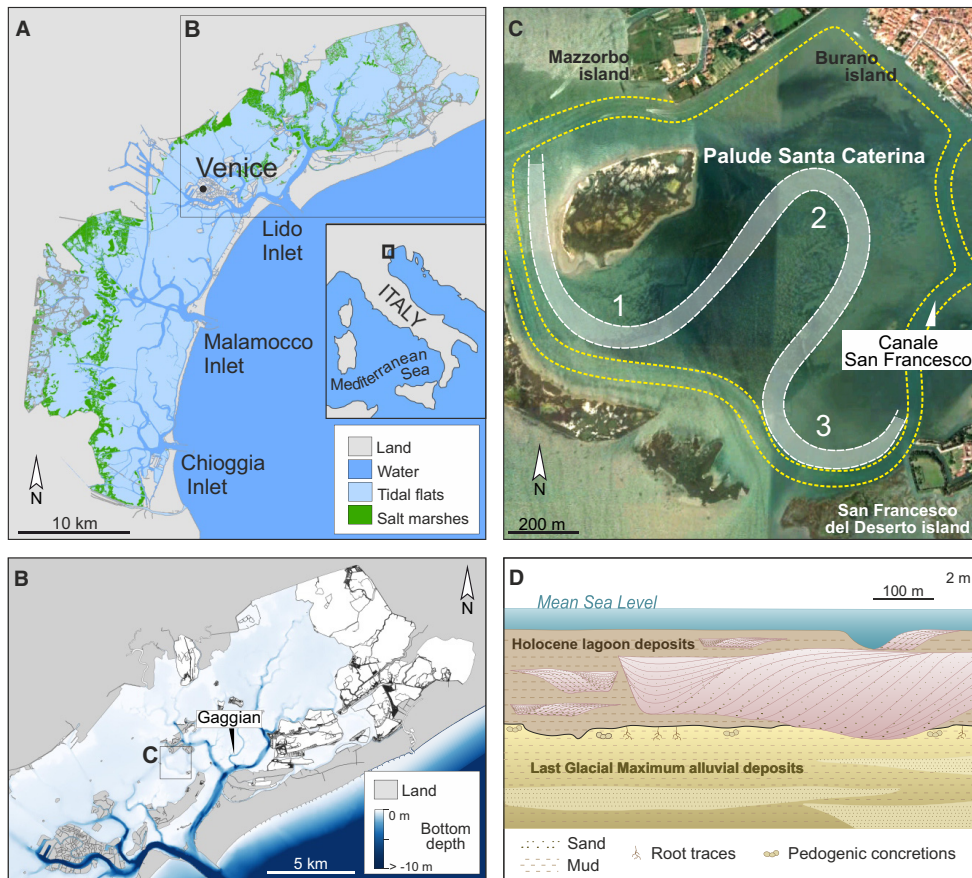

Fig. 1. The study area: (A) geographic location of the study site in the Venice Lagoon (IT); (B) bathymetric map (blue-white scale for lagoon bottom depth) of the northern Venice Lagoon; (C) Bing^TM satellite image of the Palude Santa Caterina with the three main buried meander bends reconstructed in Madricardo *et al.* (2007); and (D) hypothetical stratigraphic section of the northern Lagoon.

GEOLOGICAL SETTING

The Venice Lagoon

Covering an area of about 550 km², the Venice Lagoon is the largest brackish water body of the Mediterranean Sea; with its north-east/south-west oriented oblong and arched shape, the lagoon is 50 km long and on average 10 km wide (Zecchin *et al.*, 2008), and exchanges water with the Adriatic Sea through the Lido−San Nicolò, Malamocco and Chioggia inlets (Fig. 1A). The lagoon is affected by a semidiurnal microtidal range, with a mean tidal range and maximum astronomical oscillation of 1.0 m and 0.75 m around mean sea-level (MSL), respectively (D'Alpaos & Carniello, 2013), which can be amplified by local meteorological conditions. Low (high) atmospheric pressure can produce considerably high (low) tides. Surge events strongly contribute to enhance the astronomical tides, especially those associated with the Sirocco wind (Mel & Carniello, 2019). The Venice Lagoon is part of the Venetian foreland basin (north-east Italy), which developed between the Apennine and the South-Alpine chains (Massari *et al.*, 1986; Zecchin *et al.*, 2008). Since the Early Pleistocene, the Venice area was characterized by a shallowing-upward depositional trend from deep-water to deltaic and shoreface sediments (Massari *et al.*, 2004). These deposits were overlain by a cyclical alternation of continental and shallow-marine facies (Kent *et al.*, 2002). The Venice Lagoon developed over the last 7500 years during Holocene transgression (McClennen & Housley, 2006; Zecchin *et al.*, 2008; Rizzetto *et al.*, 2009) and consists of tidal flats, salt marshes, and subtidal and intertidal channel deposits. Sediment ranges in grain size between mud and fine sand, although mud is largely dominant (Brivio *et al.*, 2016; Ghinassi *et al.*, 2018a; Ghinassi *et al.*, 2019b). The channel network comprises tidal channels with different cross-sections, from almost 400 m to <1 m wide as the distance from the inlets rises up. Mean cross-sectional velocities within the channels can vary widely depending on the distance from the inlets and their channel width. At *ca* 6 km from the Lido inlet (Fig. 1B), the Gaggian channel and its two major tributaries (100 m and 30 to 40 m wide, respectively) show mean cross-sectional velocities of ±0.6 and ±0.4 m s⁻¹, respectively (Finotello *et al.*, 2019).

During the last centuries, human interventions contributed to modify the local tidal regime and morphologies within the lagoon (D'Alpaos, 2010; Ferrarin *et al.*, 2015). The building of massive jetties at the inlets led to their deepening and the modification of the hydrodynamic regime. The diversion of all major rivers debouching into the northern part of the Lagoon dramatically decreased the fluvial sediment input (XV to XVIII century; Tosi *et al.*, 2009; D'Alpaos, 2010; Bondesan & Furlanetto, 2012). Recently, the activation of the mobile gates (Project Mo.S.E.), designed to protect the lagoon settlements from extensive flooding, has changed the lagoon hydrodynamics (Mel *et al.*, 2021) and, consequently, the sediment transport, contributing to the deepening of the tidal flats and reducing salt-marsh sedimentation (Tognin *et al.*, 2021).

The study area

The study area is located in the northern part of the Venice Lagoon (Fig. 1B) and it is relatively close to the present-day coastline (i.e. 4 km inland). The area is right behind the S. Erasmo island, which represented the littoral strip until the end of the XIX century (Bonardi & Canal, 1997; Balletti, 2006; Busato, 2007). Specifically, the study area, named *Palude Santa Caterina,* is sited between the Burano, Mazzorbo and San Francesco del Deserto islands (Fig. 1C); it is about 1.15 km² and shows water depths ranging between 3.0 m and 0.5 m. The area is currently crossed by the *Canale San Francesco*, a 35 m wide navigable channel that exhibits three meander bends with radii of curvature ranging between 210 m and 250 m (yellow lines in Fig. 1C).

Previous geophysical and sedimentological investigations (see Madricardo *et al.*, 2007; Madricardo & Tegowski, 2012, for more details) reveal that in the study area the lagoonal Holocene succession is up to 8 m thick and covers a pedogenized alluvial substrate accumulated during the Last Glacial Maximum (Fig. 1D). The alluvial deposits consist of massive clay and fine sand layers that grade upward into over-consolidated silt, with pedogenetic nodules and roots. The lagoon deposits mainly consist of tidal-flat mud with isolated sandy to silty channelized bodies, which range in thickness between 0.5 m and 4.0 m.

Three buried palaeomeanders forming a north-west/south-east oriented belt (bends 1 to 3 in Fig. 1C) were documented in the study area (Madricardo *et al.*, 2007, 2012). These palaeomeanders were framed into a lagoonal depositional environment and associated with three sandy to silty, clinostratified point bars, which were

buried by and cut into organic-rich lagoonal mud. Specifically, point-bar deposits consist of a shell-rich lag covered by an almost 3 m thick alternation of silty-sand and sandy-silt deposits. Shells belong to lagoonal faunas, including gastropods (for example, *Bittium scabrum*) and bivalves (for example, *Acanthocardia tubercolata* and *Scrobicularia plana*) (Cosma *et al.*, 2019). The foraminiferal assemblage of bar deposits reveals that they accumulated in a subtidal setting of intermediate to inner-lagoon environment (Madricardo *et al.*, 2007, 2012), in the absence of significant riverine input. Bar-top deposits are muddy and do not show diagnostic sedimentary features of subaerial exposure in a salt marsh environment (for example, root traces and oxidation). Accordingly, their foraminiferal assemblage indicated a permanently submerged setting. Radiocarbon ages from channel lag shells date *ca* 4500 years BP (Madricardo *et al.*, 2007, 2012).

METHODS AND TERMINOLOGY

Geophysical data

The acoustic data were acquired using a single beam echosounder, modified to improve its resolution in extreme shallow waters (down to 0.5 m depth in some portions). The echosounder emits sound waves in short pulses ($\tau = 0.15$ ms) with a frequency fixed on 30 kHz, which propagate in the water down to the sea-bottom interface where the sound waves are partly reflected and partly penetrate the bottom sediments. The echosounder detects the intensity of the acoustic signals reflected from the interfaces between sediments with different properties. Despite generating a low-lateral single beam resolution in shallow water conditions, the transducer used for acquisitions provided useful data for qualitative studies thanks to its high vertical resolution, of the order of a decimetre (see Madricardo *et al.*, 2007, for more technical details). A DGPS (differential global positioning system; Trimble DSM12®; Trimble Inc., Sunnyvale, CA, USA) was associated with the echosounder, to allow a positioning accuracy of the acoustic lines below 1 m. Line spacing was set to 2.5 m and, a total of 980 sections (i.e. about 500 km of acoustic profiles in 256-level greyscale) were acquired between 2003 and 2004, allowing for investigation of the upper 6 m of the Holocene lagoonal succession. In the frame of this work, 201 sections, 2.5 to 10 m apart from one another, have been selected to reconstruct a 3D model of the subsurface succession (Fig. 2A). The *Move*
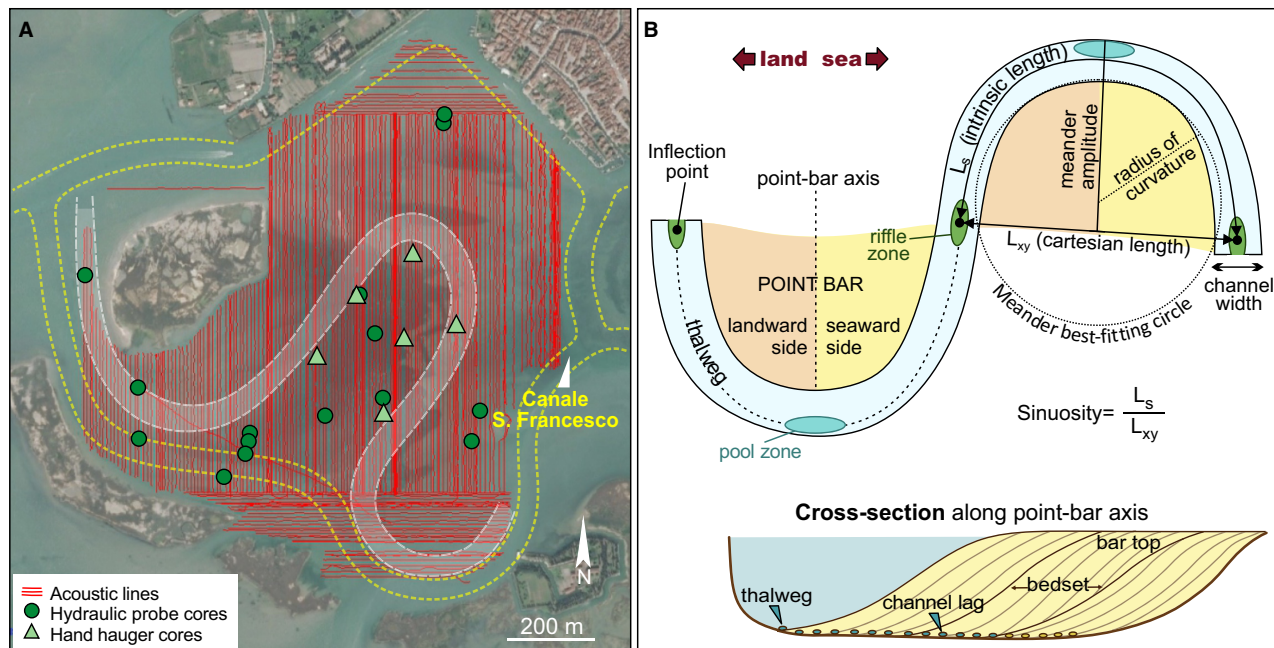

Fig. 2. Methods and terminology. (A) Location and orientation of cores and acoustic lines used in this work. (B) Main morphological, morphometric and depositional features of tidal meander bends.

2018.2^{TM} software was used to visualize and correlate different sections in a georeferenced space. The main acoustic surfaces (for example, horizons) separating different depositional elements (for example, channel-fills, channel-bars and overbank deposits) were traced for each section. Three-dimensional surfaces were created with the Ordinary Kriging method, by interpolating categories of horizons representing the same depositional element. This approach allowed the reconstruction of different stages of channel evolution and related planform configurations. Meander morphometric properties were investigated using an automatic procedure based on the computation of the channel-axis signed curvature (see Marani *et al.*, 2002; Finotello *et al.*, 2020b, for a detailed description of the methodology). Inflection points of the channel centreline, defined as curvature zero-crossings, were employed to delimit individual meander bends and allowed to determine the relevant morphometric parameters. Specifically, this study derived measures of: (i) meander Cartesian length (Lxy), defined as the Euclidean distance between meander endpoints; (ii) meander intrinsic length (Ls), i.e. computed along the channel centreline; (iii) meander sinuosity, defined as the ratio between Ls and Lxy; (iv) meander radius of curvature (R) derived from the meander best-fitting circle (see Heo *et al.*, 2009; Finotello *et al.*, 2018); and (v) meander amplitude (A) defined as the maximum distance between the channel axis and the line through the two inflection points (Fig. 2B). Changes through time of the above parameters were analysed in relation to bend 2, since the available acoustic lines did not always allow to reconstruct the complete planform of bends 1 and 3. In addition to meander planform features, thalweg depths at different bar growth stages were also marked from the acoustic sections.

Core data

A total of 21 sediment cores was used to validate geophysical data and define the spatial distribution of sedimentary facies (Fig. 2A). A hydraulic probe and a wire-line corer placed on a floating platform were used to recover 15 cores between 2004 and 2005 (Madricardo *et al.*, 2007, 2012). These cores are 10 cm in diameter and their depth spans from 8.0 to 9.1 m. The grain size was defined *in situ*, whereas lithology, sedimentary structures and Munsell colour were successively detected through laboratory analyses, where cores were sampled for micropalaeontological and radiocarbon analyses (see Madricardo *et al.*, 2007, 2012).

Six additional sedimentary cores were recovered in 2018 using an Eijkelkamp hand auger (Eijkelkamp Soil & Water, Giesbeek, The Netherlands), through a gouge sampler with a length of 1 m and a diameter of 3 cm. Coring sites were planned after preliminary results of the 3D model to analyse point-bar deposits. Coring depth spans from 4.0 to 5.8 m. Collected cores were kept humid in PVC liners and successively cut longitudinally, photographed and logged. Core logging was carried out following the basic principles of facies analysis (Walker, 1992), emphasizing sediment grain size, presence of sedimentary structures and bioturbation, vertical grain-size trends, and occurrence of plant debris and shell fragments. To verify the along-bend grain-size trend, grain-size analyses were carried out through a Mastersizer 2000 (Version 5.40, Malvern Instruments, Malvern, UK).

The terminology used in the present work is recalled in Fig. 2B and is analogous to that used for fluvial point bars and related deposits, although some modifications are required to adjust to the tidal environment (cf. Brivio *et al.*, 2016).

RESULTS

Acoustic data and architectural elements

Interpretation of acoustic profiles allowed to identify distinct acoustic facies that can be linked to three main architectural elements: channel fill, channel bar and overbank. The acoustic reflectors are interpreted to represent primary accretion and boundary surfaces (cf. Skelly & Bristow, 2003; Sambrook Smith *et al.*, 2006).

Channel bar

The channel bars are characterized by sets of packages of inclined reflectors, defined by a poorly detectable planar top and a well-marked concave-up base (Fig. 3A). They range in thickness between 2.0 m and 3.0 m starting from −1.0 m under the lagoon surface, and the inclined reflectors dip between 6° and 22° showing lateral extent up to 390 m. Channel bars show three main stratal geometries: (i) sets of packages with no internal dip changes, with cross-layered and/or oblique configuration (*sensu* Roksandic, 1978) (i.e. clinoforms) (Fig. 3A); (ii) laterally offset packages of inclined
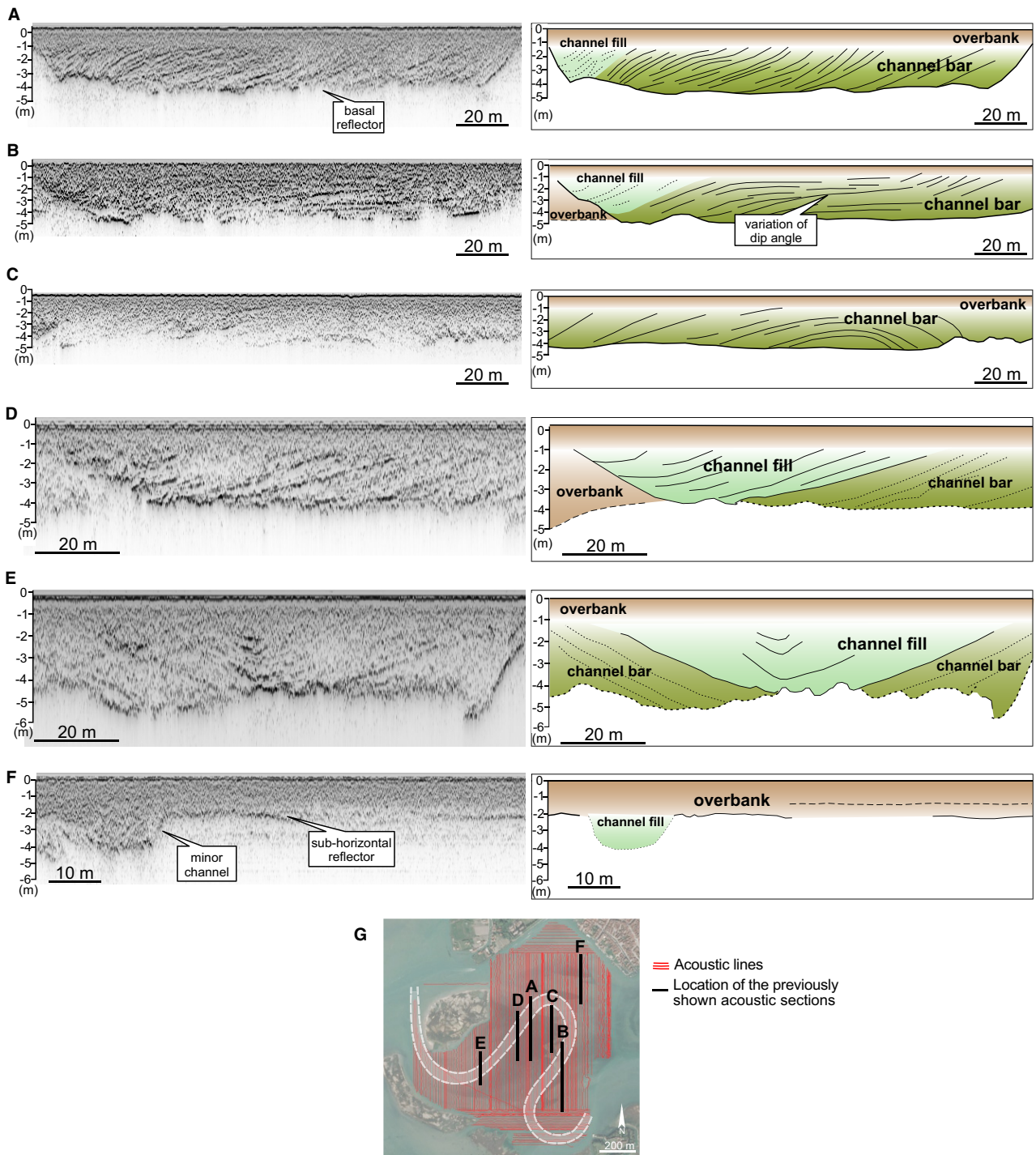
Fig. 3. Acoustic facies in the acoustic images (on the left) and with line-drawing of the preserved geometries (on the right). (A) to (C) The channel bars showing: (A) bedset packages with no internal dip changes; (B) laterally off-set packages with abrupt variations of the dip angles; and (C) mounded packages. (D) and (E) The channel fills with (D) asymmetrical and (E) symmetrical shapes. (F) The overbank with a minor channel. (G) Location of the acoustic sections chosen for the acoustic facies.

reflections showing abrupt variations either of the dip angles or in the acoustic response (Fig. 3B), with a sigmoid layer configuration (*sensu* Roksandic, 1978); and (iii) mounded package geometry with a concave-downward shape of the inclined reflections (Fig. 3C).

The clinostratified surfaces document processes of point-bar accretion related to lateral channel shift. The three stratal geometries are related to different orientations of the acoustic sections with respect to the main accretion/channel migration direction. The first geometry shows the real dip angles of the inclined reflections, in cases where the direction of accretion remained parallel to that of the acoustic section. Changes in inclination angle of acoustic reflectors document variations of the direction of accretion relative to the acoustic section. Bar accretion parallel and transverse to acoustic section generated inclined (i.e. true dip angle) and sub-horizontal reflectors, respectively. Mounded reflectors occur in sections cutting through the whole point bar and highlight its positive topographic relief.

Channel fill

Channel fills show concave-upward reflectors (Fig. 3E) and range in thickness between 1.7 m and 3.0 m, with the top surface located at approximately 1.0 m below the ground. Dip angles vary from 5° to 20°. Channel-fill reflectors can show two main geometries: (i) the asymmetrical configuration (i.e. semi-elliptical trend), which is the more common one and is always found between sets of bar reflection and overbank deposits (Fig. 3D); and (ii) the symmetrical configuration (i.e. semi-cylindrical or concentric) that is found between sets of bar reflection dipping in opposite directions (Fig. 3E).

Concave-upward reflectors testify to the progressive infill of the abandoned channel. The two geometries result from the combination between the channel orientation and that of the acoustic sections. Asymmetrical shapes are indicative of sections that are slightly oblique to the axis of the abandoned channel, whereas symmetrical ones appear in sections that are transverse to the main channel. The occurrence of symmetrical shapes between adjacent point bars is a coincidence (Fig. 3E).

Overbank

Overbanks are characterized by parallel sub-horizontal reflectors with moderate to good continuity (Fig. 3F). Localized lensoidal geometries with a basal concave upward surface can occur. These sub-horizontal reflectors represent tidal flat deposits and include localized minor channels that are too small to be imaged distinctly.

Three-dimensional reconstruction

Three-dimensional surfaces delimiting channel fills and channel bars were created to reconstruct the morphologies and orientation of the study sedimentary bodies (Fig. 4A). Minor channelized bodies (i.e. <2 m thick), though locally detected, were not modelled due to their discontinuous lateral documentation. Two channelized elements are included in the proposed 3D reconstruction and are named here as 'major' and 'minor' channels, respectively.

The major channel is that identified by Madricardo *et al.* (2007) and forms three adjacent bends with associated point-bar bodies, which are hereinafter named PB1, PB2 and PB3 (Figs 1C and 4). The channel is on average 35 m wide and channel-fill depths in pools and riffles are *ca* 3.0 m and 2.0 m, respectively.
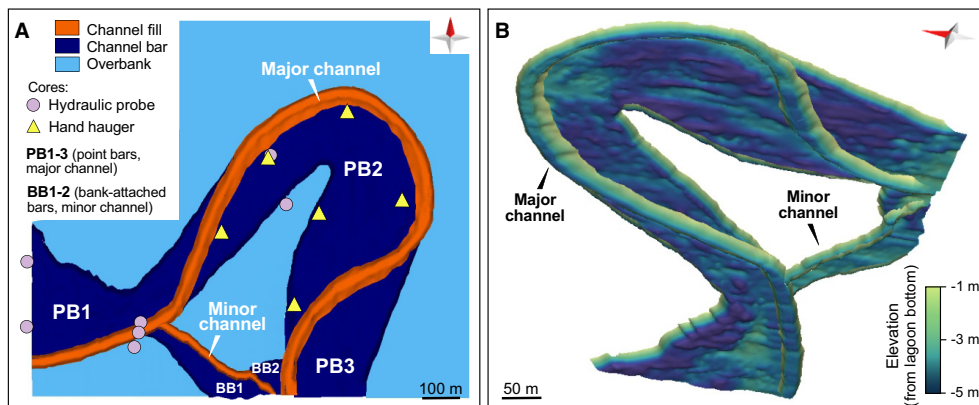

Fig. 4. Three-dimensional model. (A) Plan view of all the reconstructed surfaces and position of the analysed cores. (B) Oblique view of the palaeomeanders with elevation scale on bar surfaces.
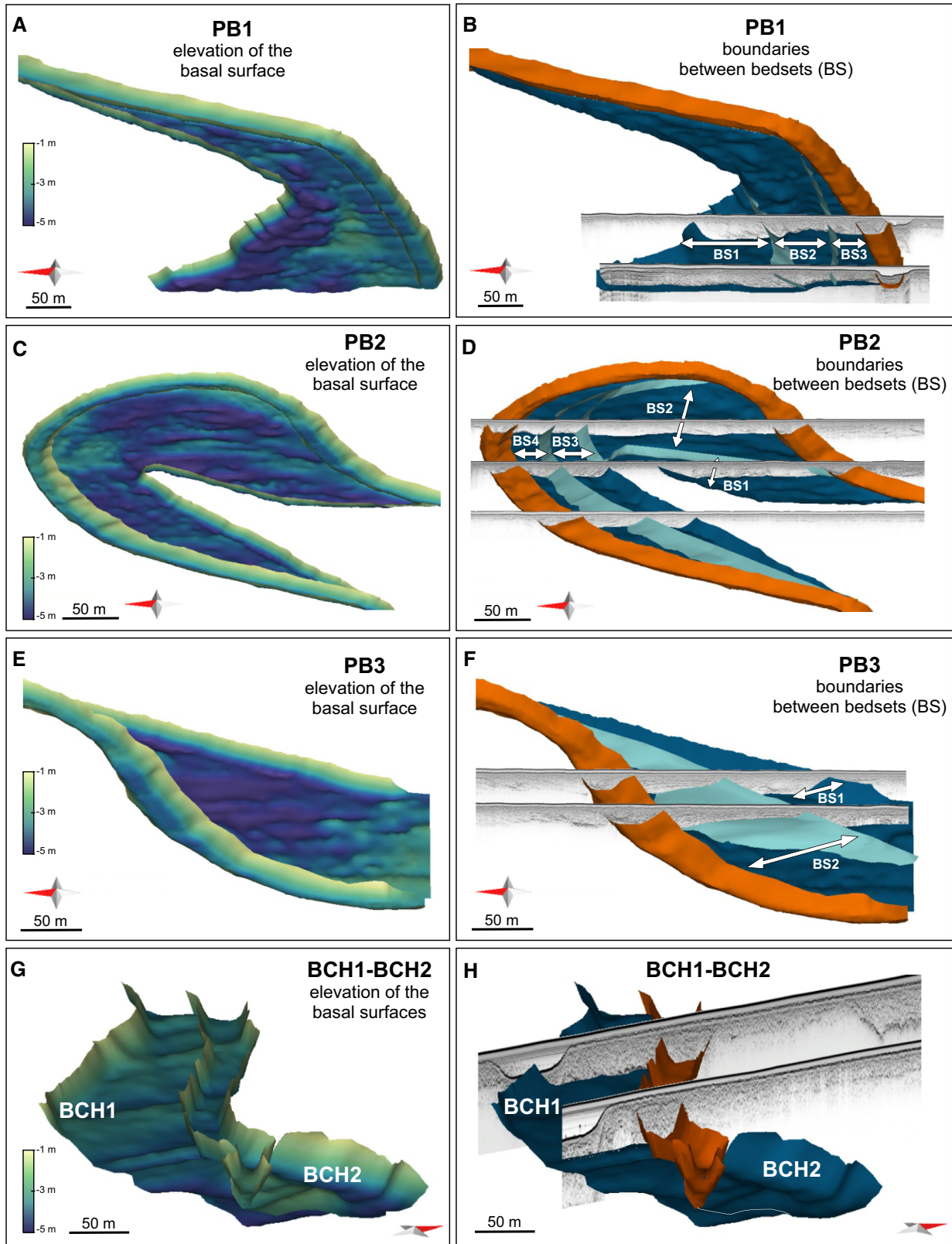
Fig. 5. Three-dimensional surfaces. (A) to (F) Point bars of the major channel with elevation scale and the corresponding portion of palaeochannel (on the left), and related internal bedsets with acoustic profiles (on the right). (G) and (H) Oblique view of the bars of the minor channel with elevation scale (G) and acoustic profiles (H).

PB1 is located in the western portion (i.e. landward sector) of the study area, but it is only partially visible and its complete geometry cannot be characterized (Figs 4A and 5A). Bar axis trends approximately north-east/south-west and deposits forming the observed part of this bar are *ca* 132 000 m³. PB1 is on average 2.6 m thick, and its thickest (3.6 m) and thinnest (1.7 m) parts occur towards the innermost and outermost part of the bar, respectively (Fig. 5A). These changes in thickness are associated with a progressive upward-shift of the bar basal surface along the direction of bar accretion, with the channel becoming shallower through time (Fig. 5A). Inclined beds forming PB1 are organized into three major bedsets (Fig. 5B) and document an overall south-west accretion of at least 200 m.

PB2 is associated with a meander bend showing an amplitude of *ca* 400 m and a radius of curvature of about 225 m. The bend axis trends north-east/south-west. The cartesian length and the intrinsic length of meander bend 2 measure *ca* 360 m and 1065 m, respectively, defining a sinuosity of 2.9. Bar deposits occupy only a limited area within the meander loop and form a U-shaped body surrounding overbank tabular beds (Fig. 4A). PB2 is on average 3 m thick, and its thickest (3.9 m) and thinnest (2.2 m) parts occur in correspondence with its major depressions and ridges, respectively (Figs 5C and 6). As for PB1, these differences in thickness are associated with an overall progressive upward-shift of the bar basal surface (Fig. 5A). The volume of sediment stored in this bar is *ca* 316 000 m³. Inclined beds of this bar are organized to form four major bedsets (BS1 to BS4 in Fig. 5D), which create arcuate bodies with a variable lateral extent on different sides of the bar. BS1 and BS2 occur along the eastward side of the bar. BS1 covers only the eastward side of the bend, whereas BS2 occurs also in the bend apex zone but shows its maximum downdip extent along the eastward side. BS3 is sited along the western side of the bar, whereas BS4 surrounds almost the whole bar, reaching its maximum downdip extent in the bar apex zone (Fig. 5D). Reconstructed morphologies of the bar basal surface show the occurrence of alternating ridges and swales, which follow the overall curvature of the associated bar and related bedsets (Fig. 5C). The major depression defined by this surface occurs below BS2, whereas its maximum elevation is associated with BS4 (Fig. 6).

PB3 is located in the easternmost portion (i.e. seaward sector) of the study area and, as for PB1, it is only partially visible (Figs 4A and 5A). Its axis trends *ca* ENE–SSW. The volume of sediments forming the observed part of PB3 is *ca* 107 000 m³. PB3 is, on average, 3 m thick, and its thickest (3.5 m) and thinnest (2.0 m) parts occur towards the innermost and outermost parts of the bar, respectively (Fig. 5E). A progressive upward-shift of the bar basal surface along the direction of accretion occurs also in PB3 (Fig. 5E). The overall direction of bar accretion is towards the west, and produced two laterally offset bedsets (Fig. 5F).

The minor channel is slightly sinuous and trends north-west/south-east connecting meanders 1 and 3 of the major channel (Fig. 4B). The minor channel is 20 m wide and the channel fill ranges in depth between 1.7 m and 2.0 m. This channel contains two bank-attached bars, which are sited along its southern (BB1) and northern (BB2) flank,
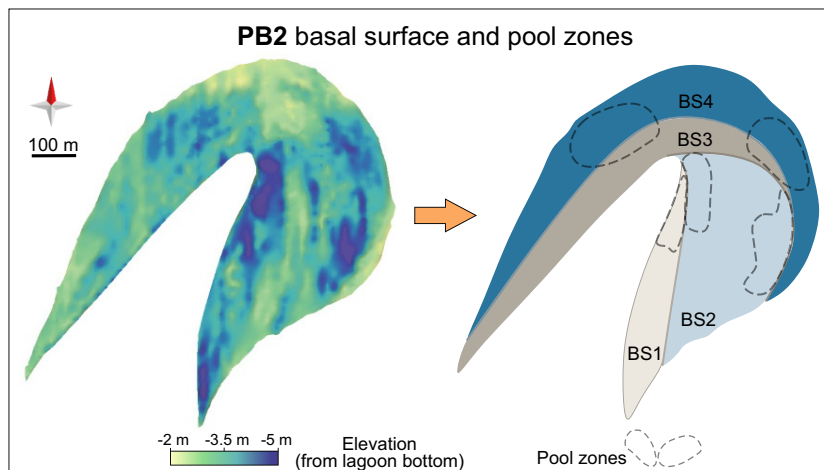

Fig. 6. Basal surface of PB2 with elevation scale to emphasize the position of pool zones within the different bedsets.

respectively (Fig. 4B). This bar typology can be found in low-sinuosity channels that do not migrate laterally enough to develop point bars, but accumulate sediment along the banks. BB1 and BB2 are characterized by north-dipping and south-dipping internal clinoforms, respectively. BB1 extends for 300 m along the entire channel (Fig. 5G). The mean thickness is 2.2 m, and it decreases to <1 m moving northward (Fig. 5H). BB2 is the smallest bar of the study area, and is found at the confluence between the minor and major channels (Fig. 4A), extending laterally for *ca* 100 m. BB2 is 3 m thick and thins to 1.7 m thick southward, where it overlaps BB1. The reconstructed volumes of BB1 and BB2 are *ca* 27 000 m³ and 6700 m³, respectively (Fig. 5H).

Core data

Sedimentary cores recovered in the area delimited by meander bend 2 allow depicting sedimentary features of PB2 and related channel-fill, along with those of the surrounding overbank deposits (Fig. 4A).

Channel-bar deposits are floored by a massive channel lag consisting of mud-free, fine sand characterized by a high content in shell fragments, with plant debris and sporadic mudclasts (Fig. 7A). Bar deposits are essentially made of silty-rich mud with subordinate 1 to 5 cm thick intervals of mud-rich very fine sand. Beds are thinly laminated with dominance of plane-parallel stratification (Fig. 7C) and local evidence of ripple cross-lamination in the sandy-rich layers (Fig. 7B). These deposits also appear locally deformed, possibly by slump processes (Fig. 7D). Scattered centimetric mudclasts are locally concentrated in sandy intervals (Fig. 7E). Plant debris is common and locally forms 1 to 5 mm thick layers (Fig. 7F). The upper part of bar deposits consists of silty-rich mud with a moderate content of plant debris (Fig. 7G) and burrows (Fig. 7H). Bar deposits are overlaid by massive tidal flat mud that is characterized by a high content of mollusc shells (*Cerastoderma glaucum* and *Bittium reticulatum*), and both bioturbations and plant debris are common (Fig. 7I).

Sedimentary cores recovered at different sites along the bar (Fig. 4A) highlight that the whole bar body does not show any relevant vertical grain-size change. Grain-size analyses from cores recovered from BS4 in the landward and seaward part of the bar do not reveal any relevant vertical or lateral (i.e. seaward or landward) change in grain size (i.e. cores SC1 to SC4 in Fig. 8).

Channel-fill deposits cover a basal silty lag and grade upward to structureless mud. Channel-fill deposits contain sporadic plant remains and mollusc shells (*B. reticulatum* and *C. glaucum*) (Fig. 9B).

Fig. 7. Sedimentary facies of point-bar deposits. (A) Lag deposits with shell fragments, plant debris and sporadic mudclasts; (B) silty-rich mud body with ripple cross-lamination in mud-rich sandy layers, (C) plane-parallel stratification and (D) slump evidence. (E) Centimetric mudclasts in sandy-rich laminae and (F) plant debris layers. (G) Upper-bar silty mud deposits with moderate content of plant debris, (H) and burrows in structureless portions. (I) Massive muddy bar-top deposits with shells (*Cerastoderma glaucum*).
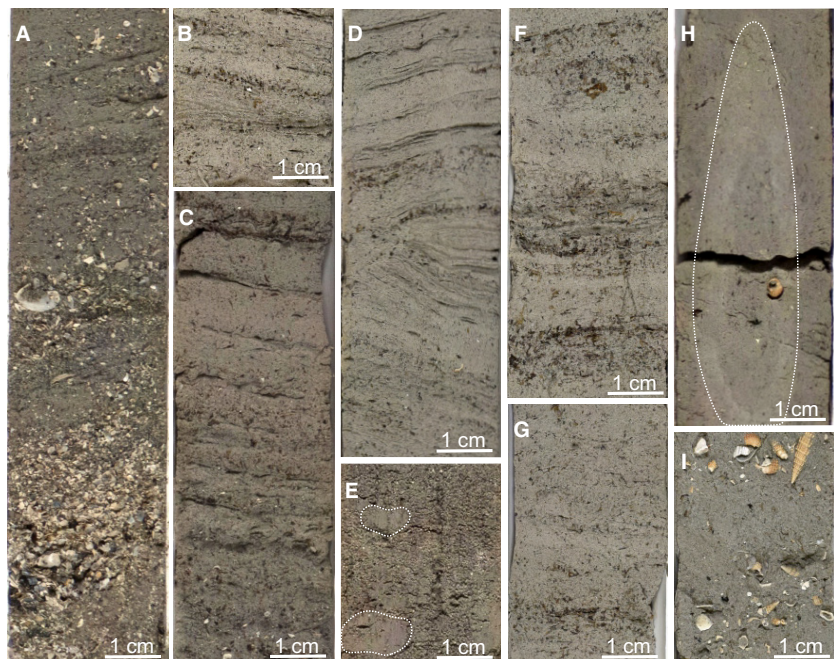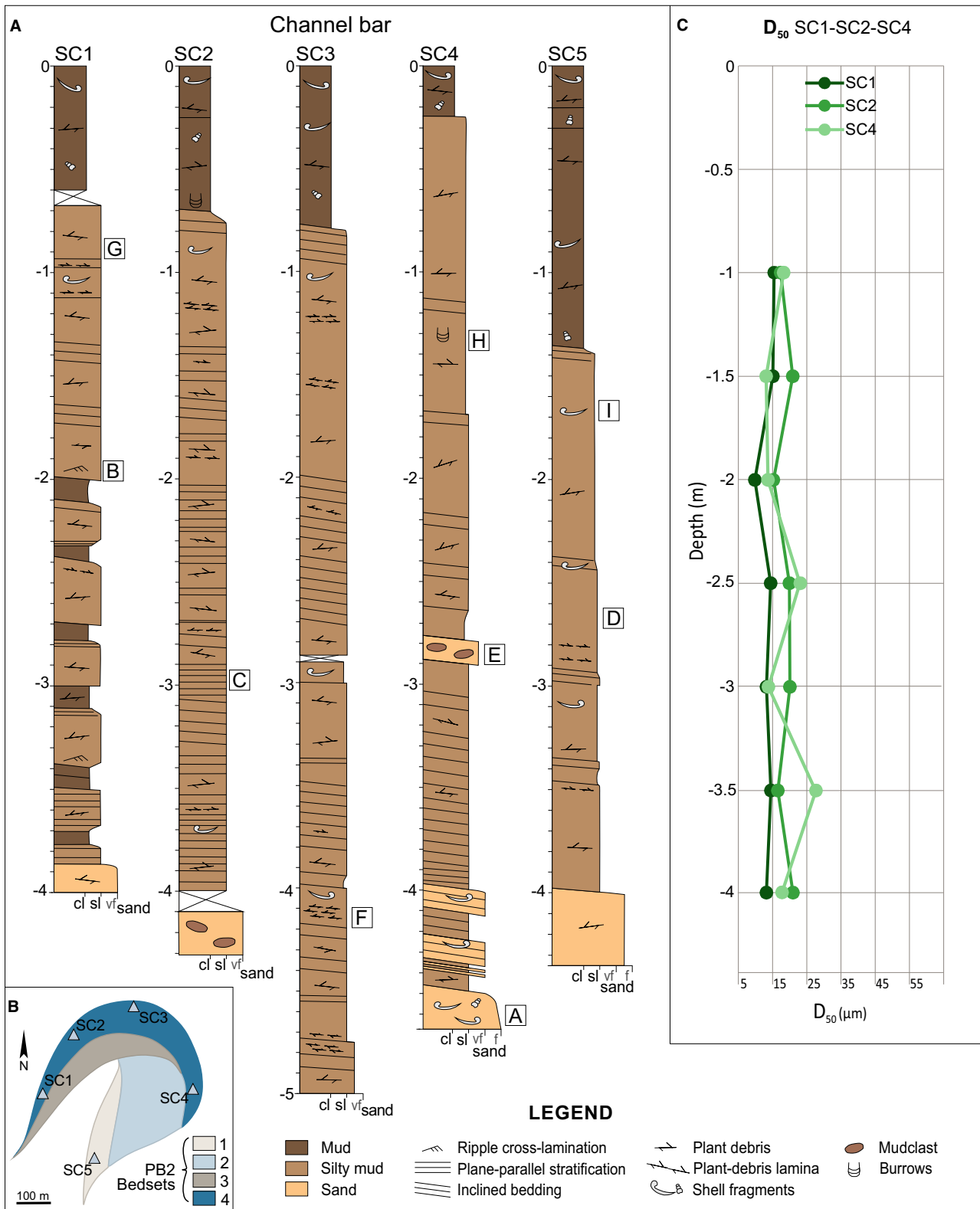
Fig. 8. Point-bar cores. (A) Stratigraphic logs and (B) core position on PB2. In inset (A), letters in squares indicate the position of the facies shown in Fig. 7. (C) Grain-size values (i.e. D_{50}) of cores SC1, SC2 and SC4.
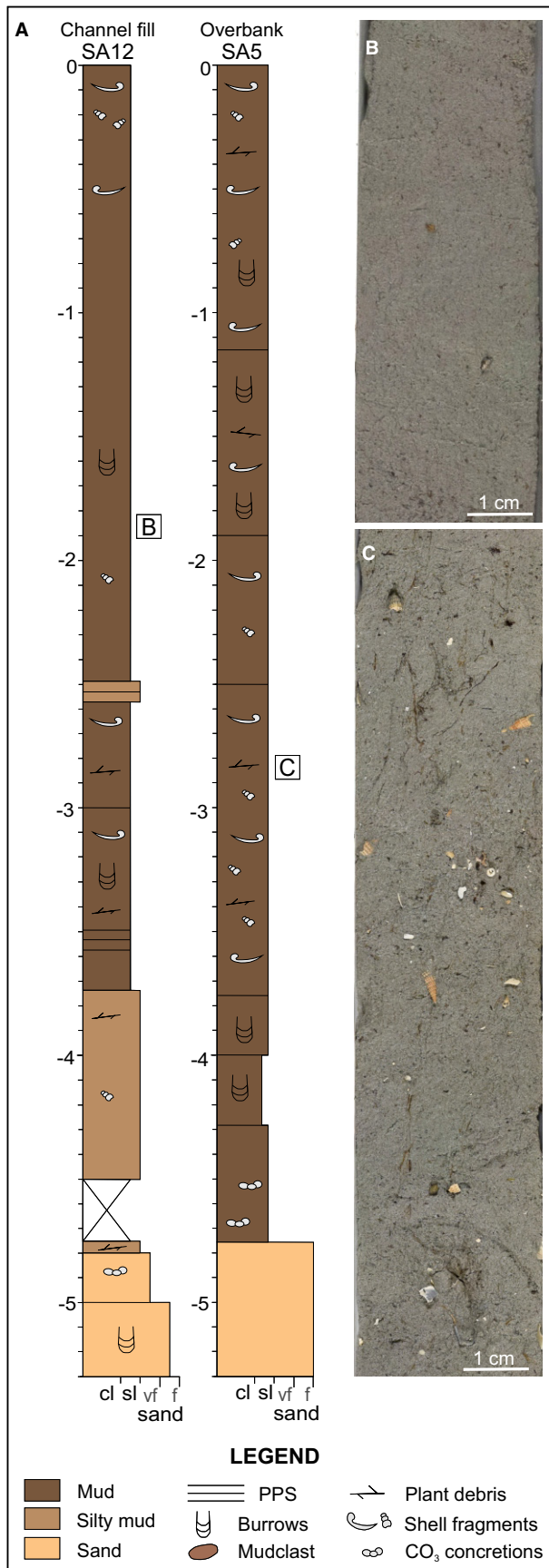
Fig. 9. Channel-fill and overbank deposits. (A) Stratigraphic logs of cores recovered within channel fill and overbank deposits; sedimentary facies of channel fill (B) and overbank (C) deposits.

Overbank deposits are mostly made of structureless mud with a high content of mollusc shells (*B. reticulatum* and *C. glaucum*) (Fig. 9C) and plant debris. These deposits do not show any evidence of subaerial exposure (for example, oxidation and root traces).

Planform evolution

Spatial distribution, orientation and curvature of different bedsets detected within the three study point bars (Fig. 5) provide the inferences which are commonly derived from the investigation of bar-top scroll pattern to reconstruct planform evolution of fluvial point bars (Ielpi & Ghinassi, 2014; Durkin *et al.*, 2015; Ielpi *et al.*, 2018; Mason & Mohrig, 2019). Bedsets are considered here as the subsurface expression of bar-top scroll-sets (Ghinassi *et al.*, 2014). Integration between architectural and sedimentological data show that accretion of point bars started from a sinuous channel and continued through four distinct stages (stages 1 to 4 in Fig. 10). The early preserved establishment stage of evolution (T0 in Fig. 11), which defined the sinuous initial morphology of the channel and was not depositional, was characterized by *Ls* and *Lxy* of meander bend 2 of 440 m and 260 m, respectively, defining a sinuosity of 1.69 (black line, Fig. 10). The meander radius of curvature and amplitude measured 134 m and 126 m, respectively, and the thalweg maximum depth value was about 1 m (Fig. 11).

During the first stage (light grey lines in Fig. 10A), meander bend 1 migrated towards the south-west with a gentle downward shift of its thalweg (Fig. 5A) and allowed the expansional accretion (*sensu* Jackson, 1976a) of the related bar with the accumulation of its first bedset package (BS1 in Fig. 5B). Simultaneously, meander bend 2 shifted eastward allowing seaward accretion (cf. Ghinassi *et al.*, 2018b) of PB2, with deposition of its first bedset, and erosion of the landward side of meander bend 3. During this stage, both *Ls* (*ca* 459 m) and *Lxy* (*ca* 270 m) of meander bend 2 slightly increased relative to the initial bend morphology (T1 in Fig. 11A). In contrast, the radius of curvature and sinuosity of the bend remained nearly constant during this
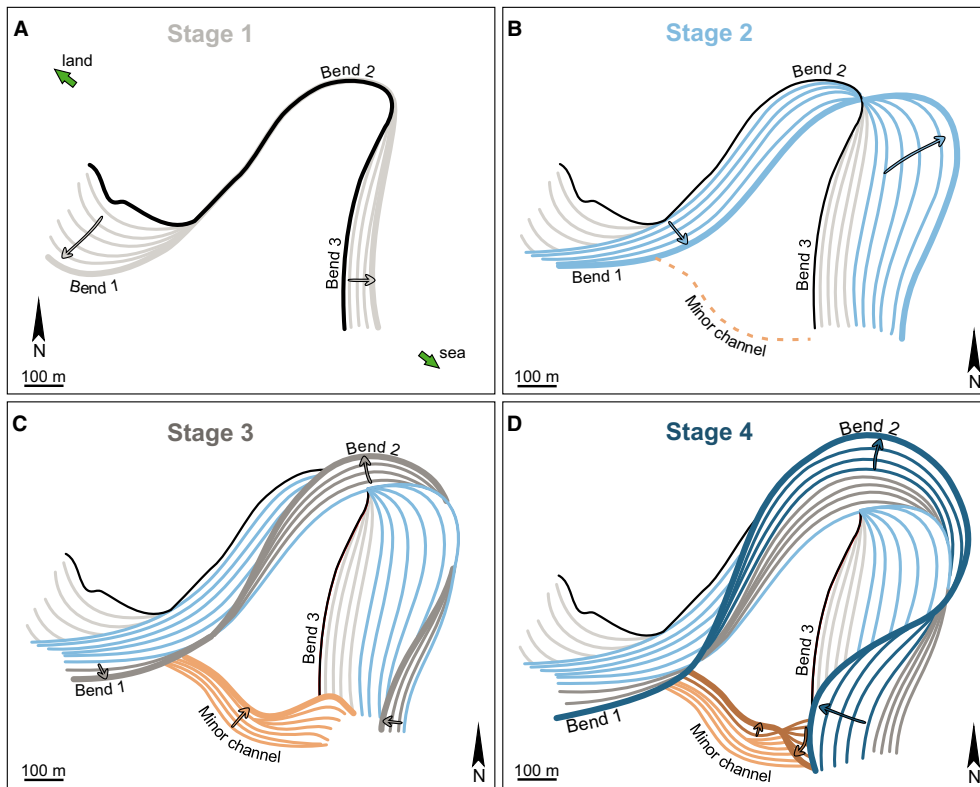
Fig. 10. Planform evolution of study channels. (A) to (D) The four stages of the reconstructed depositional evolution: (A) and (B) main seaward migration; (C) and (D) main landward accretion of the major palaeochannel with the development of the minor channel system. Arrows indicate the main directions of migration of the bars at each stage.

stage, showing values of 133 m and 1.69, with an amplitude of 144 m, respectively. During the accumulation of BS1, the channel reached a maximum depth of 4.75 m from the lagoon bottom (T1 in Fig. 11A).

During the second stage (light blue lines in Fig. 10B), meander bend 1 changed its growth pattern, experiencing an overall SSE shift that allowed PB1 to accrete accordingly and generate its second bedset package (BS2 in Fig. 5B). This stage was characterized by a marked rising of the channel thalweg (Fig. 5B). Consistently, bend 2 experienced a seaward translation, associated with a north-east migration of the bar apex, that resulted in the deposition of its second bedset package. During this second stage, meander bend 2 modified its radius of curvature from 133 m to almost 173 m and, at the end of the stage, the *Ls* and *Lxy* of meander bend 2 increased to 724 m and 360 m, respectively, producing an overall sinuosity of 2.01. Also, the meander-bend amplitude increased, doubling to 280 m (T2 in Fig. 11A). During the

accumulation of BS2, the channel reached a maximum depth of 4.92 m from the lagoon bottom (T2 in Fig. 11A) and the bar basal topography generated by thalweg shifts during this stage produced two major pool depressions close to the bend-apex zone (Fig. 6). Following meander bend 2, meander bend 3 experienced a seaward migration during this stage. Activation of the minor channel possibly occurred at this stage.

During the third depositional stage (grey lines in Fig. 10C) meander bend 1 experienced a minor SSE shift, with a gentle rising of the thalweg that generated its third bedset package (BS3 in Fig. 5B). Meander bend 2 experienced an asymmetrical growth characterized by an overall NNW landward shift and consequent accretion of the related bar through deposition of BS3. This process was associated with a partial erosion of the seaward side of bend 1. The meander bend 2 sinuosity remained almost unchanged during stage 3, but the radius of curvature increased from 173 to 199 m (T3 in Fig. 11A)
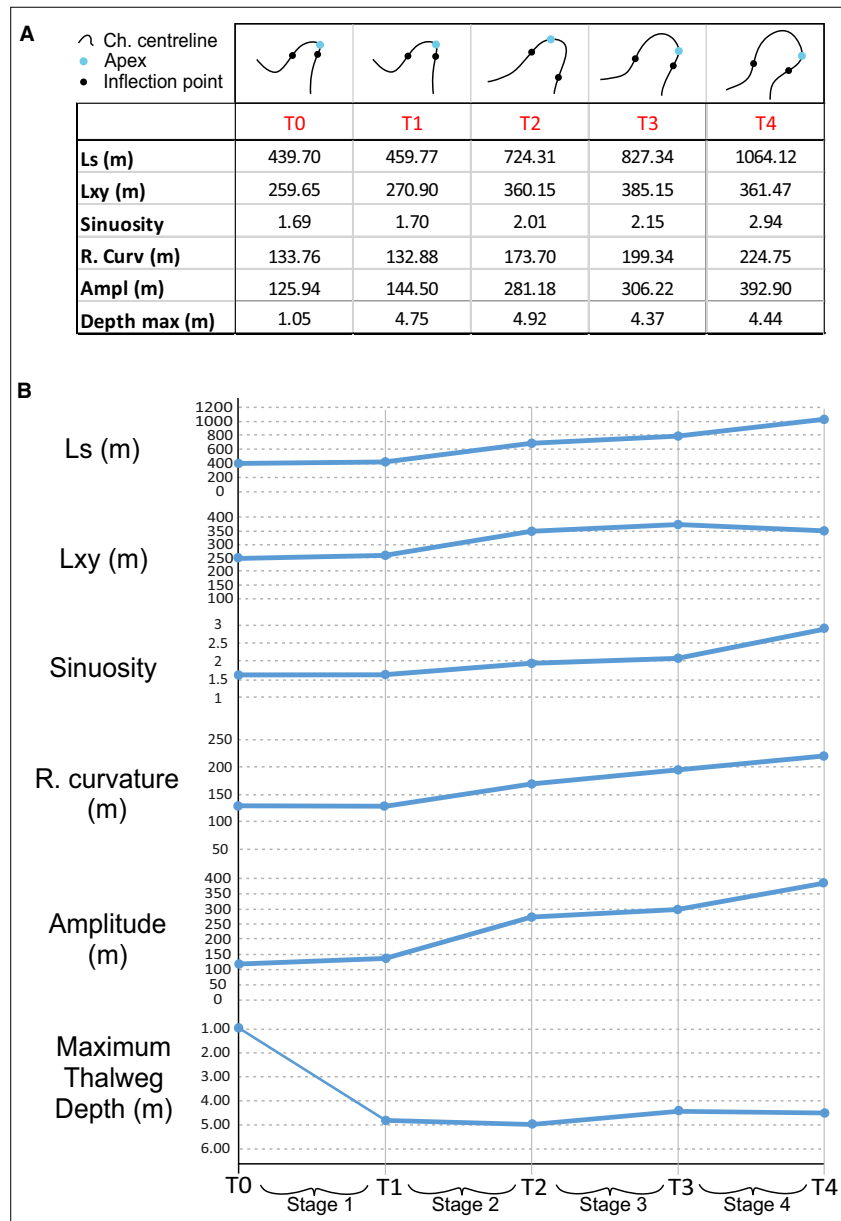
Fig. 11. Morphometric parameters and thalweg depths of meander bend 2 during the four main stages of planform evolution visualized as (A) schematic table (black lines represent the channel centreline; black and light-blue dots represent inflection points and apexes, respectively) and (B) graphs.

defining a semi-circular and more symmetrical morphology of the bend. During this stage, the *Ls* and *Lxy* increased up to 827 m and 385 m, respectively, while the meander-bend amplitude reached a value of 306 m. The maximum thalweg depth slightly rose to 4.37 m (T3 in Fig. 11A), though the available data do not offer a clear identification of the pool zone (Fig. 6). Meander bend 3 was affected by an asymmetrical growth that caused a landward accretion of the related bar, resulting in a westward shift of the channel and the consequent erosion of PB2 deposits. This growth accumulated the first preserved bedset of PB3 (BS1 in Fig. 5F). During

stage 3, the minor channel migrated towards the north-east accumulating most of the BB1 deposits (pink lines, Fig. 10C).

During stage 4 (blue lines, Fig. 10D), meander bend 1 continued to grow southward. Meander bend 2 was characterized by an asymmetrical growth towards the NNE, and consequently the final radius of curvature and sinuosity of meander bend 2 are equal to 224 m and 2.94 m, respectively. This migration leads to the increase in the *Ls* up to 1064 m, and the decrease in the cartesian length up to 361 m, whereas the meander amplitude reached the final value of 392 m (T4 in Fig. 11A). During this stage, the thalweg shift

shaped two distinct pool depressions (Fig. 6), which are separated by a ridge sited in the bend apex zone. This erosional surface floors the fourth bedset forming BD4, during which the maximum depth reached by the channel was 4.44 m from the lagoon bottom (T4 in Fig. 11A). In parallel, meander bend 3 shifted landward, leading to the accretion of PB3 and causing the erosion of PB2 deposits and accumulating the second preserved bedset package of PB3 (BS2 in Fig. 5F). The fourth depositional stage is also characterized by a minimal northward shift of the western portion of the minor channel, accreting the related deposits of BB1 (brown lines, Fig. 10D), and an abrupt growth towards the south-west of the eastern portion of the channel, which implies the deposition of BB2. This south-west shift was characterized by a marked rise of the thalweg and allowed overlap between BB1 and BB2.

Variations of the main morphometric parameters of meander bend 2 during the four morpho-dynamic stages are summarized in Fig. 11B, along with the changes of maximum thalweg depth. Although an increase in the intrinsic length of the bend clearly appears, bend evolution was also associated with a progressive increase in its cartesian length, sinuosity, amplitude and radius of curvature. The maximum thalweg depth increased by *ca* 3.5 m (from −1.0 to −4.75 m from the bottom) during the first accretionary stage (T0–T1 in Fig. 11), reaching the maximum depth during stage 2 (T1–T2 in Fig. 11). It decreased during stage 3 (from −4.92 to −4.37 m below the lagoon bottom) and remained almost constant during stage 4 (T3–T4 in Fig. 11).

DISCUSSION

Genesis and planform evolution of the bend

The overbank deposits nested within the horse-shoe point bar allow to rule out that bar accretion started from an almost straight channel, but indicate that the track of the channel was quite already sinuous (black line in Fig. 10; T0 in Fig. 11) at time of deposition inception. Accretion of PB1, PB2 and PB3 started along the inner bank of a bend, allowing PB2 to grow preserving at its core a relic of overbank mud. A similar contrast between the external geometry of meanders and the architecture of related point bars has been highlighted for fluvial meanders (Russell *et al.*, 2019) through the analysis of their complex scroll-bar patterns. Fluvial and tidal point bars are assumed to arise from a progressive increase in sinuosity of relatively straight channels (Leopold & Wolman, 1960; Daniel, 1971; Brice, 1974; Lewin, 1976; Nanson & Page, 1983; Knighton & Woodroffe, 1992; Hughes, 2012; Ghinassi *et al.*, 2014), although the planform patterns of newly-formed channels are commonly irregular, being controlled by adaptation of the flow to local micro-reliefs of the newly-drained areas (Aslan & Blum, 1999; Taylor, 1999; Motta *et al.*, 2012; Cassiani *et al.*, 2020; Bellizia *et al.*, 2021). Although adaptation of the Holocene lagoon mud to the underlying alluvial lowstand topography (Castiglioni & Favero, 1987; Amorosi *et al.*, 2008) could have generated the micro-relief required to trigger wandering of a newly-formed channel, an avulsive relocation (Slingerland & Smith, 1998, 2004; Mohrig *et al.*, 2000) of the study channel is ruled out by the lack of a significant superelevation between sub-tidal channels and surrounding overbanks. Development of such a superelevation was hindered by removal of possible levée-deposits by the combined action of waves and tidal currents (Ghinassi *et al.*, 2019b). The high density which typifies tidal networks (Marani *et al.*, 2003; Passalacqua *et al.*, 2013; Hoitink *et al.*, 2017) promotes interactions between adjacent migrating bends, causing piracies and connection of adjacent branches (Cosma *et al.*, 2020). This latter process allows the development of new creeks with a sinuous shape, which lead to a renewed circulation pattern over a pre-existing network. Where the newly-established formative discharge resulted increased by the network reorganization, an increase in the cross-sectional area of the creek (D'Alpaos *et al.*, 2010) will occur.

Reconstructed planform evolution of the study channel reveals complex patterns, which are comparable to those characterizing fluvial meanders (Daniel, 1971; Brice, 1974; Jackson, 1976b; Ielpi & Ghinassi, 2014; Yan *et al.*, 2017, 2019; Willis & Sech, 2018b). Apart from confined meanders [for example, Beaver River, Wapiti River, Red Deer River and Fontas River (Canada)] that are almost forced to translate downstream as part of a continuum of planform evolution (Lewin & Brindle, 1977; Nicoll, 2008; Nicoll & Hickin, 2010), fluvial bends behave almost independently experiencing a combination of migration styles, according to local geomorphic and sedimentary constraints, which are mainly represented by floodplain heterogeneities

(Güneralp & Rhoads, 2011; Bogoni & Putti, 2017). The study bends cut into a homogeneous, muddy overbank (Madricardo *et al.*, 2007); this lack of overbank heterogeneities hindered the development of differential planform behaviours and promoted a uniform response of the study bends to the same forcings. The restricted range of discharge, and therefore of the flowing tidal prism, and the lack of any fluvial input did not prevent the style of planform evolution from changing in time. The alternation between phases of accretion along the seaward (for example, stage 2) and landward (for example, stage 3) side of the three adjacent bends could be related to the asymmetrical character of the tidal flow. Tambroni & Luchi (2017) demonstrated that point-bar patterns in tidal meandering channels form according to the local tidal asymmetry. Tidal asymmetries control the long-term net sediment transport in tidal environments (Hoitink & Hoekstra, 2003; Van Maren & Hoekstra, 2004), with ebb (flood) dominance leading to dominant accretion of the bar along the seaward (landward) side of the bend.

In the study case, phases dominated by flood currents (for example, stage 3) were associated with erosion on the seaward side of PB2 and accretion on its landward side. Conversely, phases of ebb dominance (i.e. stage 2) were associated with erosion on the landward side of PB2 and accretion on its seaward side (cf. Ghinassi *et al.*, 2018b; Finotello *et al.*, 2019). Alternation between landward and seaward shifts of the channel contributes to shaping the planform profile of the overbank relic deposits preserved within the bar (Figs 6 and 10). Recent studies on meanders of the Venice Lagoon (Finotello *et al.*, 2019; Finotello *et al.*, 2020b) corroborated the findings of changes in sedimentation patterns with the local tidal asymmetry, and also demonstrated that morphological adaptation of meander bends to changes in local tidal asymmetry occurs over relatively short timescales (i.e. decades) even in microtidal regimes. Changes in local tidal asymmetry within tidal channels can arise both from changes in the overall structure of the tidal channel network and from modifications of the overall basin morphology. In the former instance, network modifications can happen due to meander cut-offs (Brivio *et al.*, 2016) or channel piracy events (Cosma *et al.*, 2020; Finotello *et al.*, 2020b). These processes lead to redistribution of the tidal prisms and adjustments of channel cross-section, with channel shallowing (for example, silting and infill) where the prism decreases

and cross-section enlarging where the prism increases. Such dynamics are more likely within dense networks of small channels, like those cutting through salt marshes (Marani *et al.*, 2003). Changes in local tidal asymmetry due to modifications of the basin morphology are more likely to affect larger tidal channels, especially if located in proximity of the inlets where tidal currents are more intense (Walton, 2002; Finotello *et al.*, 2019). These modifications are related to the overall morphodynamic evolution of the basin, which depends on a number of features including, for example, the inlet position and morphology, the relative extent of subtidal versus intertidal areas, the depth of tidal flat surfaces, and the position of a given channel within the basin itself, as well as possible anthropogenic influences on morphodynamics (Townend, 2010; Ferrarin *et al.*, 2015; Silvestri *et al.*, 2018; Finotello *et al.*, 2019; Guo *et al.*, 2019). Although the lack of information concerning changes of the palaeo-drainage, the size of the study palaeochannel would suggest that it suffered from the effect of a basin reorganization following a change in the inlet position, especially considering its proximity to the ancient barrier.

During the last stage of bar growth, the reducing tidal asymmetry would be consistent with a more uniform accretion along the inner bank, which was also associated with the lack of relevant changes in grain size along the bar (Fig. 8) and the development of two major pool zones along the thalweg (Fig. 6). A similar pattern of grain-size distribution and basal bar morphology has been detected in other point bars of the Venice Lagoon (Brivio *et al.*, 2016), and testifies that the seaward and landward sides of the bar alternatively experienced similar intensity of bed shear stresses over a tidal cycle, due to flood and ebb currents.

Channel morphology, thalweg trajectories and pools development

Changes of the main morphometric parameters of bend 2 during the four growth stages (Fig. 11A) are compared with changes in thalweg elevation (Fig. 11B). The overall descending, ascending and horizontal trends of the thalweg trajectory reflect adaptation of the channel to different growth stages and related flow configurations (cf. Cosma *et al.*, 2019). The initial descending trend of the thalweg (i.e. stages 1 and 2) documents the channel adjustment to its newly-established formative discharge

(Cosma *et al.*, 2019). Deep scouring was also probably promoted by the development of a bend with the lowest radius of curvature, which enhanced the erosional effects of a secondary circulation in the bend apex zone (Finotello *et al.*, 2020b). The subsequent gentle rise of the thalweg during stage 3 was probably related to the maintenance of its formative depth, which was reached at the end of stage 2. During this stage, sediments are accumulated in the channel to maintain a constant equilibrium depth in the frame of keeping dynamic equilibrium conditions (*sensu* Allen, 2000) with the surrounding aggradational tidal flats (Cosma *et al.*, 2019, 2021). This process could have also been enhanced by the activation of the minor channel, which connected bends 1 and 3 causing a local drop in the strength of erosional forces within bend 2 (cf. Toonen & Kleinhans, 2012). The almost sub-horizontal trajectory of stage 4 indicates the achievement of a new tidal prism configuration, which allowed the channel to slightly increase its depth by keeping its thalweg at a constant depth during aggradation of the surrounding tidal flats.

During the different stages of evolution, meander bend 2 developed erosive pools that are identifiable on the basal surface of PB2 as major depressions. Although stage 1 pool is not clearly defined, stage 2 shows a deep pool zone that migrates south-east following the main seaward accretion of PB2 (Fig. 6). During stage 3, the pool zone moved northward and started to show two major depocentres, which became evident in stage 4 (Fig. 6). The switching from the one-pool configuration (stages 1 and 2) to the double-pool one (stage 4) can be explained by considering the increase in the radius of curvature in a tidal cyclicity scenario. The alternate turnover of the position of impingement zones is associated with curvature-induced secondary flows, rotating in opposite directions (Finotello *et al.*, 2020b). A lower radius of curvature promotes the formation of a sharp bend where the impingement zones of flood and ebb flows against the outer bank almost coincide, causing a localized and intense scouring. In this frame, the more the radius increases, the fewer ebb and flood impingement zones against the outer bank coincide (Fig. 12). The increase in the radius of curvature caused the separation of the ebb and flood impingement zones, with the establishment of two separated zones affected by ebb and flood helical circulation, respectively (Finotello *et al.*, 2020b). Similar findings have been recently documented in a meander bend of an intertidal channel of the Venice Lagoon, sited almost 3 km east from the study area (site SC in Finotello *et al.*, 2020b), where flood and ebb flows impinge along channel banks downstream and upstream of the bend apex, respectively. This double configuration is similar to the one provided by box-shaped meanders (*sensu* Dalrymple *et al.*, 2012), and is responsible for the formation of two distinct scour pools (Hughes, 2012; Finotello, 2017) separated by a localized high (Hughes, 2012; Brivio *et al.*, 2016).

Aggradation of the minor channel

Acoustic profiles and relative 3D reconstruction also depict the stratigraphic relationship between adjacent bars in the minor channel. Here, BB2 overlaps BB1 below related channel-fill deposits (Fig. 5H), suggesting that the channel thalweg shifted southward while aggrading vertically. This vertical aggradation component of the channel trajectory (cf. Cosma *et al.*, 2019, 2020) allowed the preservation of the southern bar
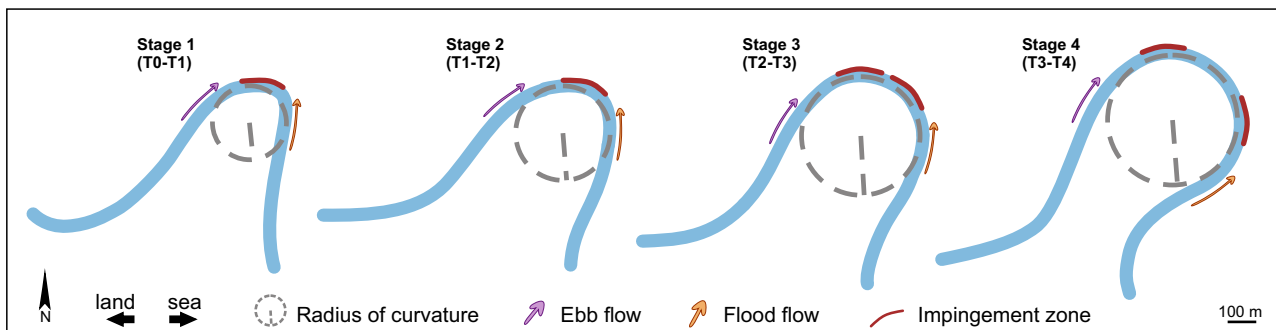

Fig. 12. Schematic representation of the variability of the radius of curvature during the four stages of palaeochannel evolution with the related position of the impingement zones.

(BB1), which was not completely dismantled by the southward channel shift. This ascending trajectory of the channel thalweg highlights that the rate of thalweg rise was sufficiently high to impact the dynamics of lateral shift of the channel. Such a configuration could derive either from the channel tendency to preserve a constant equilibrium depth under intense aggradation of overbank areas (Cosma *et al.*, 2019), or from a gradual decrease in tidal prism (Rieu *et al.*, 2005). In both cases, the occurrence of rising channel trajectories critically increases bar connectivity, as demonstrated by numerical models (Willis & Tang, 2010) and outcrop studies (Ghinassi *et al.*, 2014) for fluvial meandering rivers.

Subtidal versus intertidal point bars from the Venice Lagoon: differences and similarities

Findings of this work contribute to improve the current knowledge about subtidal meanders, by shedding some light on their morphodynamic evolution and through a comparison with their intertidal counterparts. This comparison can be carried in the frame of a similar depositional setting, that is offered here by the backbarrier basin forming the Venice Lagoon. The study case, along with a further subtidal point bar described by Ghinassi *et al.* (2019b) in the southern lagoon, provides insights on the comparison with several intertidal counterparts which were recently described (Brivio *et al.*, 2016; Ghinassi *et al.*, 2018a). In the Venice Lagoon, although all of the intertidal channels are flooded at high tides, only the smaller ones (i.e. shallower than 60–70 cm) can be completely dry at low tides, whereas the deeper ones are still partially to largely flooded. On the contrary, subtidal channels are permanently submerged also at the lowest tides. If the size of channels is similar, the grain size of point bars does not strongly differ from subtidal (Ghinassi *et al.*, 2019b) and intertidal settings (Finotello *et al.*, 2019), and channel-lag deposits seem to be ubiquitously characterized by abundance of shells and shell fragments (Brivio *et al.*, 2016; Ghinassi *et al.*, 2018a; Cosma *et al.*, 2019). Similarly, although bar deposits are laminated, no clear sedimentary structures can be detected, neither in subtidal nor in intertidal settings (Brivio *et al.*, 2016; Ghinassi *et al.*, 2018b; Cosma *et al.*, 2019). Plant-debris laminae are also widespread in both types of point bars (Brivio *et al.*, 2016; Ghinassi *et al.*, 2018b; Cosma *et al.*, 2019; Ghinassi *et al.*, 2019b). Differences occur essentially in the upper part of the bars, which show contrasting architecture and sedimentary features in subtidal and intertidal settings, respectively. The upper part of intertidal point bars is colonized by halophytic vegetation and consists of plane-parallel laminated mud (Brivio *et al.*, 2016; Ghinassi *et al.*, 2018b; Cosma *et al.*, 2019). Mud is oxidized as a consequence of repeated episodes of subaerial exposure, and bears abundant root traces (Brivio *et al.*, 2016; Ghinassi *et al.*, 2018b; Cosma *et al.*, 2019). Laminations are generally well-preserved, and commonly highlighted by the occurrence of millimetric sandy laminae, which have been commonly related to activity of wind-waves during major storm events (Brivio *et al.*, 2016; Ghinassi *et al.*, 2018b; Cosma *et al.*, 2019). Although geophysical data imaging of the transition between inclined bar slope beds and overlying sub-horizontal bar top layers are missing, this transition is associated with a gradual decrease of dip angle (Brivio *et al.*, 2016), suggesting a sigmoidal (*sensu* Gobo & Ghinassi, 2014; Gobo & Ghinassi, 2015) bar top geometry (Cosma *et al.*, 2019).

Bar top deposits in the subtidal counterparts range in grain size from mud (this study) to very-fine sand (Ghinassi *et al.*, 2019b). Despite this difference, bar-top deposits are always massive due to the intense bioturbation, and lack any evidence of oxidation. They appear generally grey to dark grey and contain abundant shells and shell fragments. Bivalves can occur in life position (Ghinassi *et al.*, 2019b). Seismic data from the southern Venice Lagoon (Ghinassi *et al.*, 2019b) show that subhorizontal bar-top beds abruptly cover inclined bar slope beds. Such an abrupt truncation was ascribed to the erosive effect of wind storm waves, which causes erosion in the bar-top area and also triggers collapses of the bar-slope deposits. Similar features were not imaged in the study site, mainly because of the low resolution of the acoustic data in the bar-top zone. The dominance of muddy deposits at the study site would be consistent with a lower efficiency of wave activity on the bar-top zone, due to the reduced wind fetch characterizing the study site during the major storm events associated with the north-east blowing Bora wind (Carniello & Defina, 2009; Carniello *et al.*, 2012; D'Alpaos *et al.*, 2013). Large waves affect the southern Venice Lagoon during these storms (Carniello *et al.*, 2009, 2012; D'Alpaos *et al.*, 2013), and account for the occurrence of erosive truncations and sandy deposits in the bar-top deposits.

CONCLUSIONS

Acoustic and sedimentary-core data allowed reconstruction of depositional patterns of deposits associated with a subtidal channel in the microtidal Venice Lagoon (Italy). The study palaeochannel was 35 m wide and 3 m deep and formed three adjacent meander bends and related point bars. A detailed 3D architectural reconstruction was carried out for deposits associated with one of these meander bends, that was crossed by a minor, low-sinuosity channel with two minor bank-attached bars.

The major insights from this 3D sedimentological reconstruction can be summarized as follows:

• The study point bar has an arcuate shape, which preserves at its core tidal-flat mud. Such a peculiar geometry was generated by the onset of bar accretion from an already sinuous channel. This process was probably triggered by the establishment of a new circulation pattern over a pre-existing network, possibly following a piracy event that connected adjacent tidal branches.

• Planform evolution of the study bend occurred through several stages that reflect asymmetrical growth of the point bars, as commonly observed in fluvial systems. This shows that, although the tidal currents work within a restricted and monotonous range of discharge, the style of bend planform evolution can change in time, possibly under the effect of variation in tidal asymmetry. Results show that under asymmetrical tidal flows, subtidal meanders develop depositional patterns according to the dominant flow direction.

• Planform transformations of the investigated bend occurred in parallel with changes in elevation of the related channel thalweg. These changes reflect the tendency of the channel to reach and maintain a specific equilibrium depth. Activation of a subordinate channel could modify the effective discharge of the major channel, influencing the vertical shift of its thalweg.

• Progressive increase in the radius of curvature of the study bend caused the splitting of the related pool scour. While the bend maintained a small radius of curvature, recirculating flows triggered by ebb end flood currents excavated the channel almost in the same area, generating a single pool depression. A progressive increase in meander-bend radius caused flood and ebb currents to create recirculation flows in different areas, with consequent development of two separated pool depressions.

• Bank-attached bars associated with the minor channel developed across the study bend migrated under aggradational conditions. This allowed overlap of these bars, which created a single and well-connected sedimentary body.

ACKNOWLEDGEMENTS

CONFLICT OF INTEREST

The authors declare that they have no competing financial or personal interests that could have appeared to influence this paper.

DATA AVAILABILITY STATEMENT

The data that support the findings of this study are openly available in Mendeley Data at https://data.mendeley.com/datasets/jpt2pd8y3h/1

REFERENCES

Allen, J.R.L. (1965) A review of the origin and characteristics of recent alluvial sediments. *Sedimentology*, **5**, 89–191.

Allen, J.R.L. (1982) *Sedimentary structures - Their character and physical basis, volume II.* Elsevier Scientific Publishing Company, Amsterdam, The Netherlands, 662 pp.

Allen, J.R.L. (2000) Morphodynamics of Holocene salt marshes: a review sketch from the Atlantic and Southern North Sea coasts of Europe. *Quat. Sci. Rev*, **19**, 1155–1231.

Amorosi, A., **Fontana, A.**, **Antonioli, F.**, **Primon, S.** and **Bondesan, A.** (2008) Post-LGM sedimentation and Holocene shoreline evolution in the NW Adriatic coastal area. *GeoActa*, **7**, 41–67.

Aslan, A. and **Blum, M.D.** (1999) Contrasting styles of Holocene avulsion, Texas Gulf coastal plain, USA. In: *Fluvial sedimentology VI: International Association of Sedimentologists Special Publication* (Eds Smith, N.D. and Rogers, J.), *Wiley Online Library*, **28**, 193–209.

Balletti, C. (2006) Digital elaborations for cartographic reconstruction: the territorial transformations of venice harbours in historical maps. *e-Perimetron*, **1**, 274–286.

Barwis, J.H. (1977) Sedimentology of some South Carolina tidal-creek point bars, and a comparison with their fluvial counterparts. *Fluv. Sedimentol*, **5**, 129–160.

Bellizia, E., **Boaga, J.**, **Fontana, A.**, **D'Alpaos, A.**, **Cassiani, G.** and **Ghinassi, M.** (2021) Impact of genesis and abandonment processes of a fluvial meander on geometry and grain-size distribution of the associated point bar (Venetian Plain, Italy). *Mar. Pet. Geol*, **127**, 104951.

Bhattacharyya, P., **Bhattacharya, J.P.** and **Khan, S.D.** (2015) Paleo-channel reconstruction and grain size variability in fluvial deposits, Ferron Sandstone, Notom Delta, Hanksville. *Utah. Sediment. Geol*, **325**, 17–25.

Bluck, B.J. (1971) Sedimentation in the meandering river Endrick. *Scottish J. Geol*, **7**, 93–138.

Bogoni, M., **Putti, M.** and **Lanzoni, S.** (2017) Modeling meander morphodynamics over self-formed heterogeneous floodplains. *Water Resour. Res*, **53**, 5137–5157.

Bonardi, M., **Canal, E.** and **Cavazzoni, S.** (1997) Sedimentological, archeological and historical evidences of paleoclimatic changes during the holocene in the lagoon of Venice (Italy). United States, 156.

Bondesan, A. and **Furlanetto, P.** (2012) Artificial fluvial diversions in the mainland of the Lagoon of Venice during the 16th and 17th centuries inferred by historical cartography analysis. *Géomorphologie Reli. Process. Environ*, **18**, 175–200.

Brice, J.C. (1974) Evolution of meander loops. *Geol. Soc. Am. Bull*, **85**, 581–586.

Bridge, J.S. (1993) Description and interpretation of fluvial deposits: a critical perspective. *Sedimentology*, **40**, 801–810.

Bridges, P.H. and **Leeder, M.R.** (1976) Sedimentary model for intertidal mudflat channels, with examples from the Solway Firth, Scotland. *Sedimentology*, **23**, 533–552.

Brivio, L., **Ghinassi, M.**, **D'Alpaos, A.**, **Finotello, A.**, **Fontana, A.**, **Roner, M.** and **Howes, N.** (2016) Aggradation and lateral migration shaping geometry of a tidal point bar: An example from salt marshes of the Northern Venice Lagoon (Italy). *Sediment. Geol*, **343**, 141–155.

Busato, D. (2007) *Metamorfosi di un litorale*. Origine e sviluppo dell'isola di Sant'Erasmo nella laguna di Venezia, Marsilio, 213 pp.

Carniello, L., **Defina, A.** and **D'Alpaos, L.** (2009) Morphological evolution of the Venice lagoon: Evidence from the past and trend for the future. *J Geophys Res Earth Surf*. **114**. https://doi.org/10.1029/2008JF001157

Carniello, L., **Defina, A.** and **D'Alpaos, L.** (2012) Modeling sand-mud transport induced by tidal currents and wind waves in shallow microtidal basins: Application to the Venice Lagoon (Italy). *Estuar. Coast. Shelf Sci.*, **102–103**, 105–115.

Cassiani, G., **Bellizia, E.**, **Fontana, A.**, **Boaga, J.**, **D'Alpaos, A.** and **Ghinassi, M.** (2020) Geophysical and Sedimentological Investigations Integrate Remote-Sensing Data to Depict Geometry of Fluvial Sedimentary Bodies: An Example from Holocene Point-Bar Deposits of the Venetian Plain (Italy). *Remote Sens*, **12**, 2568.

Castiglioni, G.B. and **Favero, V.** (1987) Linee di costa antiche ai margini orientali della Laguna di Venezia e ai lati della foce attuale del Piave. *Ist. Veneto di Sci. Lett. ed Arti, Comm. di Stud. dei Provved. per la Conserv. e Dif. della Laguna e della Città di Venezia*, 17–30.

Choi, K. (2011) Tidal rhythmites in a mixed-energy, macrotidal estuarine channel, Gomso Bay, west coast of Korea. *Mar. Geol.*, **280**, 105–115.

Choi, K., **Hong, C.M.**, **Kim, M.H.**, **Oh, C.R.** and **Jung, J.H.** (2013) Morphologic evolution of macrotidal estuarine channels in Gomso Bay, west coast of Korea: Implications for the architectural development of inclined heterolithic stratification. *Mar. Geol.*, **346**, 343–354.

Choi, K.S. and **Jo, J.H.** (2015) Morphodynamics of Tidal Channels in the Open Coast Macrotidal Flat, Southern Ganghwa Island in Gyeonggi Bay, West Coast of Korea. *J. Sediment. Res.*, **85**, 582–595.

Clement, W.P. and **Barrash, W.** (2006) Crosshole radar tomography in a fluvial aquifer near Boise, Idaho. *J. Environ. Eng. Geophys*, **11**, 171–184.

Clift, P.D., **Olson, E.D.**, **Lechnowskyj, A.**, **Moran, M.G.**, **Barbato, A.** and **Lorenzo, J.M.** (2019) Grain-size variability within a mega-scale point-bar system, False River, Louisiana. *Sedimentology*, **66**, 408–434.

Cosma, M., **Finotello, A.**, **Ielpi, A.**, **Ventra, D.**, **Oms, O.**, **D'Alpaos, A.** and **Ghinassi, M.** (2020) Piracy-controlled geometry of tide-dominated point bars: Combined evidence from ancient sedimentary successions and modern channel networks. *Geomorphology*, **370**, 107402.

Cosma, M., **Ghinassi, M.**, **D'Alpaos, A.**, **Roner, M.**, **Finotello, A.**, **Tommasini, L.** and **Gatto, R.** (2019) Point-bar brink and channel thalweg trajectories depicting interaction between vertical and lateral shifts of microtidal channels in the Venice Lagoon (Italy). *Geomorphology*, **342**, 37–50.

Cosma, M., **Yan, N.**, **Colombera, L.**, **Mountney, N.P.**, **D'Alpaos, A.** and **Ghinassi, M.** (2021) An integrated approach to determine three-dimensional accretion geometries of tidal point bars: Examples from the Venice Lagoon (Italy). *Sedimentology*, **68**, 449–476.

D'Alpaos, A., **Carniello, L.** and **Rinaldo, A.** (2013) Statistical mechanics of wind wave-induced erosion in shallow tidal basins: Inferences from the Venice Lagoon. *Geophys. Res. Lett*, **40**, 3402–3407.

D'Alpaos, A., **Lanzoni, S.**, **Marani, M.** and **Rinaldo, A.** (2010) On the tidal prism-channel area relations. *J. Geophys. Res. Earth Surf*, **115**, 1–13.

D'Alpaos, L. (2010) *Fatti e misfatti di idraulica lagunare. La laguna di Venezia dalla diversione dei fiumi alle nuove opere delle bocche di porto*. IVSLA, Istituto Veneto di Scienze, Lettere ed Arti, Venice, 355 pp.

Dalrymple, R.W. and **Choi, K.** (2007) Morphologic and facies trends through the fluvial-marine transition in tide-dominated depositional systems: A schematic framework for environmental and sequence-stratigraphic interpretation. *Earth-Science Rev.*, **81**, 135–174.

Dalrymple, R.W., **Knight, R.J.**, **Zaitlin, B.A.** and **Middleton, G.V.** (1990) Dynamics and facies model of a macrotidal

sand-bar complex, Cobequid Bay—Salmon River Estuary (Bay of Fundy). *Sedimentology*, **37**, 577–612.

Dalrymple, R.W., **Mackay, D.A.**, **Ichaso, A.A.** and **Choi, K.S.** (2012) Processes, morphodynamics, and facies of tide-dominated estuaries. In: *Principles of Tidal Sedimentology* (Eds Davis, R.A. and Dalrymple, R.W.), pp. 79–107. Springer.

Daniel, J.F. (1971) *Channel Movement of Meandering Indiana Streams*, 732nd edn. US Government Printing Office, Washington, DC.

Durkin, P.R., **Boyd, R.L.**, **Hubbard, S.M.**, **Shultz, A.W.** and **Blum, M.D.** (2017) Three-dimensional reconstruction of meander-belt evolution, Cretaceous McMurray Formation, Alberta foreland basin, Canada. *J. Sediment. Res*, **87**, 1075–1099.

Durkin, P.R., **Hubbard, S.M.**, **Boyd, R.L.** and **Leckie, D.A.** (2015) Stratigraphic expression of intra-point-bar erosion and rotation. *J. Sediment. Res*, **85**, 1238–1257.

Fabbri, P., **Ortombina, M.** and **Piccinini, L.** (2012) Estimation of Hydraulic Conductivity Using the Slug Test Method in a Shallow Aquifer in the Venetian Plain (NE, Italy). *Aqua Mundi.*, **3**, 125–133.

Fagherazzi, S., **Gabet, E.J.** and **Furbish, D.J.** (2004) The effect of bidirectional flow on tidal channel planforms. *Earth Surf. Process. Landforms*, **29**, 295–309.

Ferrarin, C., **Tomasin, A.**, **Bajo, M.**, **Petrizzo, A.** and **Umgiesser, G.** (2015) Tidal changes in a heavily modified coastal wetland. *Cont. Shelf Res*, **101**, 22–33.

Finotello, A. (2017) *Tidal Channel Patterns: Field Investigations, Numerical Modelling and Laboratory Experiments*. University of Padova, Padova.

Finotello, A., **Canestrelli, A.**, **Carniello, L.**, **Ghinassi, M.** and **D'Alpaos, A.** (2019) Tidal Flow Asymmetry and Discharge of Lateral Tributaries Drive the Evolution of a Microtidal Meander in the Venice Lagoon (Italy). *J. Geophys. Res. Earth Surf*, **124**, 3043–3066.

Finotello, A., **D'Alpaos, A.**, **Bogoni, M.**, **Ghinassi, M.** and **Lanzoni, S.** (2020a) Remotely-sensed planform morphologies reveal fluvial and tidal nature of meandering channels. *Sci. Rep*, **10**, 1–13.

Finotello, A., **Ghinassi, M.**, **Carniello, L.**, **Belluco, E.**, **Pivato, M.**, **Tommasini, L.** and **D'Alpaos, A.** (2020b) Three-dimensional flow structures and morphodynamic evolution of microtidal meandering channels. *Water Resour. Res.*, **56**, e2020WR027822.

Finotello, A., **Lanzoni, S.**, **Ghinassi, M.**, **Marani, M.**, **Rinaldo, A.** and **D'Alpaos, A.** (2018) Field migration rates of tidal meanders recapitulate fluvial morphodynamics. *Proc. Natl. Acad. Sci*, **115**, 1463–1468.

Flemming, B.W. (2012) Siliciclastic Back-Barrier Tidal Flats. In: *Principles of Tidal Sedimentology* (Eds Davis, R.A.J. and Dalrymple, R.W.), pp. 231–267. Springer, Dordrecht.

Frings, R.M. (2008) Downstream fining in large sand-bed rivers. *Earth-Science Rev*, **87**, 39–60.

Fustic, M., **Hubbard, S.M.**, **Spencer, R.**, **Smith, D.G.**, **Leckie, D.A.**, **Bennett, B.** and **Larter, S.** (2012) Recognition of down-valley translation in tidally influenced meandering fluvial deposits, Athabasca Oil Sands (Cretaceous), Alberta,Canada. *Mar. Pet. Geol*, **29**, 219–232.

Gabet, E. (1998) Lateral Migration and Bank Erosion in a Saltmarsh. *Estuaries*, **21**, 745–753.

Gershenzon, N.I., **Ritzi Jr, R.W.**, **Dominic, D.F.**, **Soltanian, M.**, **Mehnert, E.** and **Okwen, R.T.** (2015) Influence of small-scale fluvial architecture on CO_2 trapping processes in deep brine reservoirs. *Water Resour. Res*, **51**, 8240–8256.

Ghinassi, M., **Billi, P.**, **Libsekal, Y.**, **Papini, M.** and **Rook, L.** (2013) Inferring fluvial morphodynamics and overbank flow control from 3D outcrop sections of a Pleistocene point bar, Dandiero Basin, Eritrea. *J. Sediment. Res*, **83**, 1065–1083.

Ghinassi, M., **Brivio, L.**, **D'Alpaos, A.**, **Finotello, A.**, **Carniello, L.**, **Marani, M.** and **Cantelli, A.** (2018a) Morphodynamic evolution and sedimentology of a microtidal meander bend of the Venice Lagoon (Italy). *Mar. Pet. Geol*, **96**, 391–404.

Ghinassi, M., **Colombera, L.**, **Mountney, N.P.** and **Reesink, A.J.H.** (2019) Sedimentology of meandering river deposits: advances and challenges. In: *Fluvial Meanders and Their Sedimentary Products in the Rock Record, Int. Assoc. Sedimentol. Spec. Publ.* (Eds Ghinassi, M., Colombera, L. and Mountney, N.P.), *Wiley-Blackwell*, **48**, 1–14.

Ghinassi, M., **D'alpaos, A.**, **Gasparotto, A.**, **Carniello, L.**, **Brivio, L.**, **Finotello, A.**, **Roner, M.**, **Franceschinis, E.**, **Realdon, N.**, **Howes, N.** and **Cantelli, A.** (2018b) Morphodynamic evolution and stratal architecture of translating tidal point bars: Inferences from the northern Venice Lagoon (Italy). *Sedimentology*, **65**, 1354–1377.

Ghinassi, M., **D'Alpaos, A.**, **Tommasini, L.**, **Brivio, L.**, **Finotello, A.** and **Stefani, C.** (2019) Tidal currents and wind waves controlling sediment distribution in a subtidal point bar of the Venice Lagoon (Italy). *Sedimentology*, **66**, 2926–2949.

Ghinassi, M. and **Ielpi, A.** (2015) Stratal architecture and morphodynamics of downstream-migrating fluvial point bars (Jurassic Scalby Formation, UK). *J. Sediment. Res*, **85**, 1123–1137.

Ghinassi, M., **Ielpi, A.**, **Aldinucci, M.** and **Fustic, M.** (2016) Downstream-migrating fluvial point bars in the rock record. *Sediment. Geol*, **334**, 66–96.

Ghinassi, M., **Nemec, W.**, **Aldinucci, M.**, **Nehyba, S.**, **Özaksoy, V.** and **Fidolini, F.** (2014) Plan-form evolution of ancient meandering rivers reconstructed from longitudinal outcrop sections. *Sedimentology*, **61**, 952–977.

Gobo, K., **Ghinassi, M.** and **Nemec, W.** (2014) Reciprocal changes in foreset to bottomset facies in a gilbert-type delta: Response to short-term changes in base level. *J. Sediment. Res*, **84**, 1079–1095.

Gobo, K., **Ghinassi, M.** and **Nemec, W.** (2015) Gilbert-type deltas recording short-term base-level changes: Delta-brink morphodynamics and related foreset facies. *Sedimentology*, **62**, 1923–1949.

Güneralp, Í. and **Rhoads, B.L.** (2011) Influence of floodplain erosional heterogeneity on planform complexity of meandering rivers. *Geophys. Res. Lett*, **38**, 2–7.

Guo, L., **Wang, Z.B.**, **Townend, I.** and **He, Q.** (2019) Quantification of tidal asymmetry and its nonstationary variations. *J. Geophys. Res. Ocean*, **124**, 773–787.

Hagstrom, C.A., **Hubbard, S.M.**, **Leckie, D.A.** and **Durkin, P.R.** (2019) The effects of accretion-package geometry on lithofacies distribution in point-bar deposits. *J. Sediment. Res*, **89**, 381–398.

Heo, J., **Duc, T.A.**, **Cho, H.S.** and **Choi, S.U.** (2009) Characterization and prediction of meandering channel migration in the GIS environment: A case study of the Sabine River in the USA. *Environ. Monit. Assess*, **152**, 155–165.

Hoitink, A.J.F., **Hoekstra, P.** and **Van Maren, D.S.** (2003) Flow asymmetry associated with astronomical tides: Implications for the residual transport of sediment. *J. Geophys. Res. Ocean*, **108**, 1–8.

Hoitink, A.J.F., **Wang, Z.B.**, **Vermeulen, B.**, **Huismans, Y.** and **Kästner, K.** (2017) Tidal controls on river delta morphology. *Nat. Geosci*, **10**, 637–645.

Hubbard, S.M., **Smith, D.G.**, **Nielsen, H.**, **Leckie, D.A.**, **Fustic, M.**, **Spencer, R.J.** and **Bloom, L.** (2011) Seismic geomorphology and sedimentology of a tidally influenced river deposit, Lower Cretaceous Athabasca oil sands, Alberta, Canada. *Am. Assoc. Pet. Geol. Bull*, **95**, 1123–1145.

Hughes, Z.J. (2012) Tidal channels on tidal flats and marshes. In: *Principles of Tidal Sedimentology* (Eds Davis, R.A. and Dalrymple, R.W.), pp. 269–300. Springer, New York.

Ielpi, A. and **Ghinassi, M.** (2014) Planform architecture, stratigraphic signature and morphodynamics of an exhumed Jurassic meander plain (Scalby Formation, Yorkshire, UK). *Sedimentology*, **61**, 1923–1960.

Ielpi, A., **Ghinassi, M.**, **Rainbird, R.H.** and **Ventra, D.** (2018) Planform sinuosity of Proterozoic rivers: A craton to channel-reach perspective. In: *Fluvial Meanders and Their Sedimentary Products in the Rock Record. Int. Assoc. Sedimentol. Spec. Publ. 48* (Eds Ghinassi, M., Colombera, L., Mountney, N.P., Reesink, A.J. and Bateman, M.), pp. 81–118. John Wiley & Sons Ltd, Chichester, West Sussex, UK.

Issautier, B., **Viseur, S.**, **Audigane, P.** and **Le Nindre, Y.-M.** (2014) Impacts of fluvial reservoir heterogeneity on connectivity: Implications in estimating geological storage capacity for CO2. *Int. J. Greenh. Gas Control*, **20**, 333–349.

Jackson, R.G. (1976a) Largescale ripples of the lower Wabash River. *Sedimentology*, **23**, 593–623.

Jackson, R.G. (1976b) Depositional model of point bars in the lower Wabash River. *J. Sediment. Res.*, **46**, 579–594.

Janocko, M., **Nemec, W.**, **Henriksen, S.** and **Warchoł, M.** (2013) The diversity of deep-water sinuous channel belts and slope valley-fill complexes. *Mar. Pet. Geol*, **41**, 7–34.

Kent, D.V., **Rio, D.**, **Massari, F.**, **Kukla, G.** and **Lanci, L.** (2002) Emergence of Venice during the Pleistocene. *Quat. Sci. Rev.*, **21**, 1719–1727.

Knighton, A.D., **Woodroffe, C.D.** and **Mills, K.** (1992) The evolution of tidal creek networks, Mary River, northern Australia. *Earth Surf. Process. Landforms*, **17**, 167–190.

Kolla, V., **Posamentier, H.W.** and **Wood, L.J.** (2007) Deep-water and fluvial sinuous channels-Characteristics, similarities and dissimilarities, and modes of formation. *Mar. Pet. Geol*, **24**, 388–405.

La Croix, A.D. and **Dashtgard, S.E.** (2015) A synthesis of depositional trends in intertidal and upper subtidal sediments across the tidal–fluvial transition in the Fraser River, Canada. *J. Sediment. Res*, **85**, 683–698.

Leopold, L.B. and **Wolman, M.G.** (1960) River Meanders. *Geol. Soceity Am. Bull*, **71**, 769–793.

Lewin, J. (1976) Initiation of bed forms and meanders in coarse-grained sediment. *Bull. Geol. Soc. Am*, **87**, 281–285.

Lewin, J. and **Brindle, B.J.** (1977) Confined meanders. In: *River Channel Changes* (Ed. Gregory, K.J.), pp. 221–233. John Wiley and Sons, Chichester.

Li, C., **Chen, C.**, **Guadagnoli, D.** and **Georgiou, I.Y.** (2008) Geometry-induced residual eddies in estuaries with curved channels: Observations and modeling studies. *J. Geophys. Res*, **113**, C01005.

Madricardo, F., **Donnici, S.**, **Lezziero, A.**, **De Carli, F.**, **Buogo, S.**, **Calicchia, P.** and **Boccardi, E.** (2007) Palaeoenvironment reconstruction in the Lagoon of Venice through wide-area acoustic surveys and core sampling, Estuar. *Coast. Shelf Sci.*, **75**, 205–213.

Madricardo, F., **Tegowski, J.** and **Donnici, S.** (2012) Automated detection of sedimentary features using wavelet analysis and neural networks on single beam echosounder data: A case study from the Venice Lagoon, Italy. *Cont. Shelf Res*, **43**, 43–54.

Marani, M., **Belluco, E.**, **D'Alpaos, A.**, **Defina, A.**, **Lanzoni, S.** and **Rinaldo, A.** (2003) On the drainage density of tidal networks. *Water Resour. Res*, **39**, 1040.

Marani, M., **Lanzoni, S.**, **Zandolin, D.**, **Seminara, G.** and **Rinaldo, A.** (2002) Tidal meanders. *Water Resour. Res*, **38**, 7–14.

Mason, J. and **Mohrig, D.** (2019) Scroll bars are inner bank levees along meandering river bends. *Earth Surf. Process. Landforms*, **44**, 2649–2659.

Massari, F., **Grandesso, P.**, **Stefani, C.** and **Jobstraibizer, P.G.** (1986) A small polyhistory foreland basin evolving in a context of oblique convergence: the Venetian basin (Chattian to Recent, Southern Alps, Italy). In: *Foreland Basins* (Eds Allen, P.A. and Homewood, P.), pp. 141–168. Blackwell Scientific, Oxford.

Massari, F., **Rio, D.**, **Serandrei Barbero, R.**, **Asioli, A.**, **Capraro, L.**, **Fornaciari, E.** and **Vergerio, P.P.** (2004) The environment of Venice area in the past two million years. *Palaeogeogr. Palaeoclimatol. Palaeoecol*, **202**, 273–308.

McClennen, C.E. and **Housley, R.A.** (2006) Late-holocene channel meander migration and mudflat accumulation rates, lagoon of venice, Italy. *J. Coast. Res*, **22**, 930–945.

Mel, R., **Carniello, L.** and **D'Alpaos, L.** (2019) Addressing the effect of the Mo.S.E. barriers closure on wind setup within the Venice lagoon. *Estuar. Coast. Shelf Sci*, **225**, 106249.

Mel, R.A., **Viero, D.P.**, **Carniello, L.**, **Defina, A.** and **D'Alpaos, L.** (2021) The first operations of Mo.S.E. system to prevent the flooding of Venice: Insights on the hydrodynamics of a regulated lagoon. *Estuar. Coast. Shelf Sci*, **261**, 107547.

Mohrig, D., **Heller, P.L.**, **Paola, C.** and **Lyons, W.J.** (2000) Interpreting avulsion process from ancient alluvial sequences: Guadalope-Matarranya system (Northern Spain) and Wasatch formation (Western Colorado). *Geol. Soc. Am. Bull*, **112**, 1787–1803.

Motta, D., **Abad, J.D.**, **Langendoen, E.J.** and **García, M.H.** (2012) The effects of floodplain soil heterogeneity on meander planform shape. *Water Resour. Res*, **48**, 1–17.

de Mowbray, T. (1983) The genesis of lateral accretion deposits in recent intertidal mudflat channels, Solway Firth, Scotland. *Sedimentology*, **30**, 425–435.

Nanson, G.C. (1980) Point bar and floodplain formation of the meandering Beatton River, northeastern British Columbia, Canada. *Sedimentology*, **27**, 3–29.

Nanson, G.C. and **Page, K.** (1983) Lateral accretion of fine-grained concave benches on meandering rivers. In: *Modern and ancient fluvial systems. Int. Assoc. Sedimentol. Spec. Publ.* (Eds Collinson, J.D. and Lewin, J.), *Wiley-Blackwell*, **6**, 133–143.

Nicoll, T. (2008) *Planform Geometry and Kinematics of Confined Meandering Rivers on the Canadian Prairies*. Simon Fraser University, Burnaby, Canada.

Nicoll, T.J. and **Hickin, E.J.** (2010) Planform geometry and channel migration of confined meandering rivers on the Canadian prairies. *Geomorphology*, **116**, 37–47.

Parquer, M., **Yan, N.**, **Colombera, L.**, **Mountney, N.**, **Collon, P.** and **Caumon, G.** (2019) Combined inverse and forward numerical models of fluvial meandering-channel evolution and facies distributions. In: *34th IAS meeting of Sedimentology*, 1.

Passalacqua, P., Lanzoni, S., Paola, C. and Rinaldo, A. (2013) Geomorphic signatures of deltaic processes and vegetation: The Ganges-Brahmaputra-Jamuna case study. *J Geophys Res Earth Surf*, **118**(3), 1838–1849. https://doi.org/10.1002/jgrf.20128

Pearson, N.J. and Gingras, M.K. (2006) An Ichnological and sedimentological facies model for muddy point-bar deposits. *J. Sediment. Res*, **76**, 771–782.

Posamentier, H.W. (2003) Depositional elements associated with a basin floor channel-levee system: Case study from the Gulf of Mexico. *Mar. Pet. Geol*, **20**, 677–690.

Pranter, M.J., Ellison, A.I., Cole, R.D. and Patterson, P.E. (2007) Analysis and modeling of intermediate-scale reservoir heterogeneity based on a fluvial point-bar outcrop analog, Williams Fork Formation, Piceance Basin, Colorado. *Am. Assoc. Pet. Geol. Bull*, **91**, 1025–1051.

Purkait, B. (2002) Patterns of Grain-Size Distribution in Some Point Bars of the Usri River, India. *J. Sediment. Res*, **72**, 367–375.

Rieu, R., Van Heteren, S., Van der Spek, A.J.F. and De Boer, P. (2005) Development and preservation of a mid-Holocene tidal-channel network offshore the western Netherlands. *J. Sediment. Res*, **75**, 409–419.

Rizzetto, F., Tosi, L., Brancolini, G., Zecchin, M., Baradello, L. and Tan, C. (2009) Ancient geomorphological features in shallows of the Venice Lagoon (Italy). *J. Coast. Res*, **56**, 752–756.

Roksandic, M.M. (1978) Seismic facies analysis concepts. *Geophys. Prospect*, **26**, 383–398.

Russell, C.E., Mountney, N.P., Hodgson, D.M. and Colombera, L. (2019) A novel approach for prediction of lithological heterogeneity in fluvial point-bar deposits from analysis of meander morphology and scroll-bar pattern. In: *Fluvial Meanders and Their Sedimentary Products in the Rock Record. Int. Assoc. Sedimetol. Spec. Publ.* (Eds Ghinassi, M., Colombera, L., Mountney, N.P. and Reesink, J.H.), **48**, 385–418.

Sambrook Smith, G.H., Ashworth, P.J., Best, J.L., Woodward, J. and Simpson, C.J. (2006) The sedimentology and alluvial architecture of the sandy braided South Saskatchewan River, Canada. *Sedimentology*, **53**, 413–434.

Silvestri, S., D'Alpaos, A., Nordio, G. and Carniello, L. (2018) Anthropogenic Modifications Can Significantly Influence the Local Mean Sea Level and Affect the Survival of Salt Marshes in Shallow Tidal Systems. *J. Geophys. Res. Earth Surf*, **123**, 996–1012.

Skelly, R.L., Bristow, C.S. and Ethridge, F.G. (2003) Architecture of channel-belt deposits in an aggrading shallow sandbed braided river: The lower Niobrara River, northeast Nebraska. *Sediment. Geol*, **158**, 249–270.

Slingerland, R. and Smith, N.D. (1998) Necessary conditions for a meandering-river avulsion. *Geology*, **26**, 435–438.

Slingerland, R. and Smith, N.D. (2004) River avulsions and their deposits. *Annu. Rev. Earth Planet. Sci*, **32**, 257–285.

Smith, D.G., Hubbard, S.M., Leckie, D.A. and Fustic, M. (2009) Counter point bar deposits: Lithofacies and reservoir and ancient McMurray formation, Alberta, Canada. *Sedimentology*, **56**, 1655–1669.

Smith, D.G., Hubbard, S.M., Lavigne, J.R., Leckie, D.A. and Fustic, M. (2011) Stratigraphy of counter-point-bar and eddy-accretion deposits in low-energy meander belts of the Peace-Athabasca Delta, northeast Alberta, Canada. In:

From River to Rock Record: The Preservation of Fluvial Sediments and Their Subsequent Interpretation (Eds Davidson, S.K., Leleu, S. and North, C.P.), *SEPM Special Publication*, **97**, 143–152.

Strick, R.J.P., Ashworth, P.J., Awcock, G. and Lewin, J. (2018) Morphology and spacing of river meander scrolls. *Geomorphology*, **310**, 57–68.

Tambroni, N., Luchi, R. and Seminara, G. (2017) Can tide dominance be inferred from the point bar pattern of tidal meandering channels? *J. Geophys. Res. Earth Surf*, **122**, 492–512.

Taylor, C.F.H. (1999) The role of overbank flow in governing the form of an anabranching river: the Fitzroy River, northwestern Australia. In: *Fluvial Sedimentology VI. Special Publication of the International Association of Sedimentologists* (Eds Smith, N.D. and Rogers, J.), *Wiley Online Library*, **28**, 77–91.

Tognin, D., D'Alpaos, A., Marani, M. and Carniello, L. (2021) Marsh resilience to sea-level rise reduced by storm-surge barriers in the Venice Lagoon. *Nat. Geosci.*, **14**, 906–911. https://doi.org/10.1038/s41561-021-00853-7

Tommasini, L., Carniello, L., Ghinassi, M., Roner, M. and D'Alpaos, A. (2019) Changes in the wind-wave field and related salt-marsh lateral erosion: inferences from the evolution of the Venice Lagoon in the last four centuries. *Earth Surf. Process. Landforms*, **44**, 1633–1646.

Toonen, W.H.J., Kleinhans, M.G. and Cohen, K.M. (2012) Sedimentary architecture of abandoned channel fills. *Earth Surf. Process. Landforms*, **37**, 459–472.

Tosi, L., Rizzetto, F., Zecchin, M., Brancolini, G. and Baradello, L. (2009) Morphostratigraphic framework of the Venice Lagoon (Italy) by very shallow water VHRS surveys: Evidence of radical changes triggered by human-induced river diversions. *Geophys. Res. Lett*, **36**, 1–5.

Townend, I. (2010) An exploration of equilibrium in Venice Lagoon using an idealised form model. *Cont. Shelf Res*, **30**, 984–999.

Van Maren, D.S., Hoekstra, P. and Hoitink, A.J.F. (2004) Tidal flow asymmetry in the diurnal regime: Bed-load transport and morphologic changes around the Red River Delta. *Ocean Dyn*, **54**, 424–434.

Visher, G.S. (1964) Fluvial processes as interpreted from ancient and recent fluvial deposits. *Am. Assoc. Pet. Geol. Bull*, **48**, 550.

Walker, R.G. (1992) Facies, facies models and modern stratigraphic concepts. In: *Facies models: Response to sea-level change* (Eds Walker, R.G. and James, N.P.), pp. 272–314. Geological Association of Canada, Toronto.

Walton, T.L. (2002) Tidal velocity asymmetry at inlets.

Willis, B.J. (1989) Palaeochannel reconstructions from point bar deposits: a three-dimensional perspective. *Sedimentology*, **36**, 757–766.

Willis, B.J. and Sech, R.P. (2018a) Quantifying impacts of fluvial intra-channel-belt heterogeneity on reservoir behaviour. In: *Fluvial Meanders and Their Sedimentary Products in the Rock Record (Int. Assoc. Sedimentol. Spec. Publ. 48)* (Eds Ghinassi, M., Colombera, L., Mountney, N.P. and Reesink, A.J.H.), pp. 543–572. John Wiley & Sons, Chichester, West Sussex, UK.

Willis, B.J. and Sech, R.P. (2018b) Emergent facies patterns within fluvial channel belts. In: *Fluvial Meanders and Their Sedimentary Products in the Rock Record. Int. Assoc. Sedimentol. Spec. Publ.* (Eds Ghinassi, M., Colombera, L., Mountney, N.P., Reesink, A.J.H. and Bateman, M.), *John Wiley & Sons, Ltd*, **48**, 509–542.

Willis, B.J. and **Tang, H.** (2010) Three-Dimensional Connectivity of Point-Bar Deposits. *J. Sediment. Res*, **80**, 440–454.

Yan, N., **Colombera, L.**, **Mountney, N.P.** and **Dorrell, R.M.** (2019) Fluvial point-bar architecture and facies heterogeneity, and their influence on intra-bar static connectivity in humid coastal-plain and dryland fan systems. In: *Fluvial Meanders and Their Sedimentary Products in the Rock Record (IAS SP 48)* (Eds Ghinassi, M., Colombera, L., Mountney, N.P. and Reesink, A.J.H.), pp. 475–508. John Wiley & Sons.

Yan, N., **Mountney, N.P.**, **Colombera, L.** and **Dorrell, R.M.** (2017) A 3D forward stratigraphic model of fluvial meander-bend evolution for prediction of point-bar lithofacies architecture. *Comput. Geosci*, **105**, 65–80.

Zecchin, M., **Baradello, L.**, **Brancolini, G.**, **Donda, F.**, **Rizzetto, F.** and **Tosi, L.** (2008) Sequence stratigraphy based on high-resolution seismic profiles in the late Pleistocene and Holocene deposits of the Venice area. *Mar. Geol.*, **253**, 185–198.